Author Manuscript

Author Manuscript

Author Manuscript

Author Manuscript

HHS Public Access

Author manuscript

*Cancer Cell*. Author manuscript; available in PMC 2021 May 11.

Published in final edited form as:

*Cancer Cell*. 2020 May 11; 37(5): 655–673.e11. doi:10.1016/j.ccell.2020.04.004.

# MUTANT EZH2 INDUCES A PRE-MALIGNANT LYMPHOMA NICHE BY REPROGRAMMING THE IMMUNE RESPONSE

**Wendy Béguelin**[1,*], **Matt Teater**[1,2], **Cem Meydan**[2], **Kenneth B. Hoehn**[3], **Jude M. Phillip**[1], **Alexey A. Soshnev**[4], **Leandro Venturutti**[1], **Martín A. Rivas**[1], **María T. Calvo-Fernández**[1], **Johana Gutierrez**[1], **Jeannie M. Camarillo**[5], **Katsuyoshi Takata**[6], **Karin Tarte**[7], **Neil L. Kelleher**[5], **Christian Steidl**[6], **Christopher E. Mason**[2,8,9,10], **Olivier Elemento**[2,8], **C. David Allis**[4], **Steven H. Kleinstein**[3,11], **Ari M. Melnick**[1,*,#]

[1]Division of Hematology/Oncology, Department of Medicine, Weill Cornell Medicine, Cornell University, New York, NY 10021, USA

[2]Institute for Computational Biomedicine, Weill Cornell Medicine, Cornell University, New York, NY 10021, USA

[3]Department of Pathology, Yale School of Medicine, New Haven, CT 06520, USA

[4]Laboratory of Chromatin Biology and Epigenetics, The Rockefeller University, New York, NY 10065, USA

[5]Department of Chemistry, Molecular Biosciences and the National Resource for Translational and Developmental Proteomics, Northwestern University, Evanston, IL 60208, USA

[6]Center for Lymphoid Cancer, British Columbia Cancer, Vancouver, BC V5Z 1L3, Canada

[7]UMR 1236, Université Rennes 1, INSERM, Etablissement Français du Sang, 35043 Rennes, France

[8]Department of Physiology and Biophysics, Weill Cornell Medicine, Cornell University, New York, NY, 10021, USA

[9]The WorldQuant Initiative for Quantitative Prediction, Weill Cornell Medicine, New York, NY 10021, USA

[*]**Correspondence:** web2002@med.cornell.edu, amm2014@med.cornell.edu.

[#]Lead Contact

AUTHOR CONTRIBUTIONS

Conceptualization: W.B., A.M.M.; methodology: W.B., M.T., C.M., K.B.H., J.P., N.L.K., S.H.K; software and formal analysis: M.T., C.M., K.B.H., J.P., J.M.C., N.L.K., C.E.M, O.E., S.H.K.; investigation: W.B., A.A.S., L.V., M.A.R., M.T.C., J.G., K.Takata; resources: N.L.K., C.S., C.E.M., O.E., C.D.A., S.H.K.; data curation: M.T., C.M., K.B.H.; writing – original draft: W.B., A.M.M.; writing – review & editing: W.B., A.M.M., J.P., L.V., K.B.H., S.H.K., C.D.A., C.E.M., K.Tarte; visualization: W.B., M.T., C.M., K.B.H., J.P., J.M.C.; project administration: W.B.; funding acquisition: A.M.M.

**Publisher's Disclaimer:** This is a PDF file of an unedited manuscript that has been accepted for publication. As a service to our customers we are providing this early version of the manuscript. The manuscript will undergo copyediting, typesetting, and review of the resulting proof before it is published in its final form. Please note that during the production process errors may be discovered which could affect the content, and all legal disclaimers that apply to the journal pertain.

DECLARATION OF INTERESTS

A.M.M. is consulting for Epizyme and Constellation Pharmaceuticals, and receives research funding from Janssen Pharmaceuticals; S.H.K. is consulting for Northrop Grumman; C.E.M. is a co-founder and equity stake holder for Onegevity Health and Biotia, Inc; C.S. has performed consultancy for Seattle Genetics, Curis Inc., Roche, AbbVie, Juno Therapeutics and Bayer, and has received research funding from Bristol-Myers Squibb and Trillium Therapeutics Inc. There are no competing interests.

Author Manuscript Author Manuscript Author Manuscript Author Manuscript

[10]The Feil Family Brain and Mind Research Institute, Weill Cornell Medicine, New York, NY 10021, USA

[11]Interdepartmental Program in Computational Biology and Bioinformatics, Yale University, New Haven, CT 06511, USA

## SUMMARY

Follicular lymphomas (FL) are slow-growing, indolent tumors containing extensive follicular dendritic cell (FDC) networks and recurrent *EZH2* gain-of-function mutations. Paradoxically, FLs originate from highly proliferative germinal center (GC) B cells with proliferation strictly dependent on interactions with T follicular helper cells. Herein, we show that *EZH2* mutations initiate FL by attenuating GC B cell requirement for T cell help and driving slow expansion of GC centrocytes that become enmeshed with and dependent on FDCs. By impairing T cell help, mutant EZH2 prevents induction of proliferative MYC programs. Thus, *EZH2* mutation fosters malignant transformation by epigenetically reprograming B cells to form an aberrant immunological niche that reflects characteristic features of human FLs, explaining how indolent tumors arise from GC B cells.

## Graphical Abstract

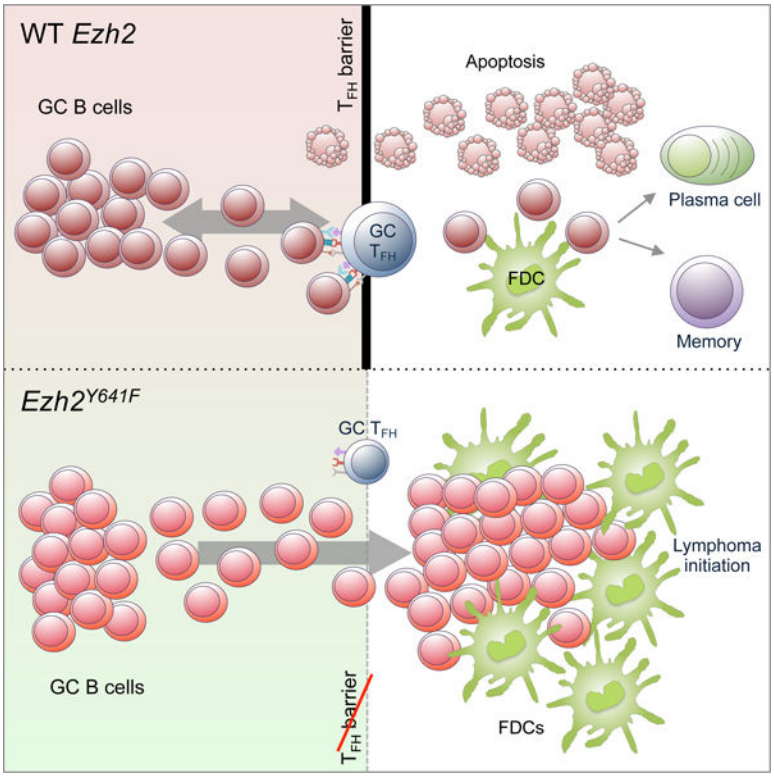


## IN BRIEF

Béguelin et al. show that mutant EZH2 epigenetically reprograms germinal center B cells to alter their interactions with T follicular helper cells and follicular dendritic cells, facilitating malignant

Author Manuscript Author Manuscript Author Manuscript Author Manuscript

transformation and establishing characteristic features of the follicular lymphoma immunological niche.

**Keywords**

Follicular lymphoma; EZH2; germinal center; immune microenvironment; epigenetic dysregulation

## INTRODUCTION

Follicular lymphomas (FLs) are the second most common form of B cell lymphoma and generally present as indolent and relatively slow growing tumors (Scott and Gascoyne, 2014). In spite of this, most FLs are incurable and eventually transform into aggressive and refractory high-grade lymphomas (Lossos and Gascoyne, 2011). FLs originate from germinal center (GC) B cells, which are among the most rapidly dividing cell types. GCs are transient structures within which B cells undergo massive proliferation and somatic hypermutation of their immunoglobulin loci. The densely packed region of proliferating B cells (named centroblasts) is called the GC dark zone (DZ) (Mlynarczyk et al., 2019; Victora and Nussenzweig, 2012). After several rounds of division, GC B cells stop proliferating to become centrocytes that form the GC “light zone” (LZ) together with T follicular helper (Tfh) and follicular dendritic cells (FDCs). Within the LZ, GC B cells compete to interact with limiting numbers of Tfh cells, based on the affinity of their B cell receptor (i.e., immunoglobulin genes) for antigen (Mesin et al., 2016). Most GC B cells fail to receive T cell help and undergo apoptosis. The few that receive T cell help either return to the DZ for additional rounds of proliferation and mutagenesis (a MYC-dependent process called GC recycling), or exit the GC reaction to form antibody-secreting plasma cells (Mesin et al., 2016).

The typical histological appearance of low-grade FL is that of enlarged lymphoid follicles containing aberrant centrocytes, highly enmeshed within a network of FDC processes and variable numbers of T cells (Lossos and Gascoyne, 2011). It is not known how these aberrant lymphoid follicles evolve from normal GCs. One especially puzzling aspect of FL pathogenesis is the apparent paradox of how highly proliferative GC B cells could transform into indolent and slowly proliferative tumors. It is also notable that even though centrocytes are highly T cell dependent, FLs are generally resistant to T cell augmentation therapies such as checkpoint inhibitors (Kline et al., 2019). One source of clues that could help to address such questions are the genetic lesions that occur in FL. For example, gain-of-function mutations of the *EZH2* histone methyltransferase occur in 25–30% of FL patients, as well as in GCB-like diffuse large B cell lymphomas (Bodor et al., 2013; Chapuy et al., 2018; Morin et al., 2010; Okosun et al., 2014; Reddy et al., 2017; Schmitz et al., 2018). The vast majority of these alleles encode a single amino acid substitution affecting the Y641 residue within the EZH2 catalytic domain. $EZH2^{Y641}$ mutants are far more efficient than WT enzyme in converting H3K27me2 to H3K27me3 (Sneeringer et al., 2010; Yap et al., 2011). Hence, $EZH2^{Y641}$ mutant cell lines or GC B cells manifest increased abundance of

Author Manuscript Author Manuscript Author Manuscript Author Manuscript

the H3K27me3 repressive histone mark (Beguelin et al., 2013; Beguelin et al., 2016; Souroullas et al., 2016).

Under normal conditions, *EZH2* is upregulated in GC B cells and required for GC formation (Beguelin et al., 2013; Caganova et al., 2013; Velichutina et al., 2010). Critical functions of WT EZH2 in GC B cells include repression of cell cycle checkpoint and differentiation genes to support centroblast proliferation and prevent premature plasma cell differentiation (Beguelin et al., 2017). These repressive effects of EZH2 resolve as B cells exit the GC reaction. Exposure of *EZH2* mutant or WT diffuse large B cell lymphomas to EZH2 inhibitors leads to proliferation arrest and plasma cell differentiation (Beguelin et al., 2013; Brach et al., 2017; Knutson et al., 2012; McCabe et al., 2012b), which raises the question of whether *EZH2* mutation has any additional qualitatively distinct function in lymphomagenesis beyond simply being a more potent version of the WT enzyme. In fact, the effect of *EZH2* mutation on malignant transformation of GC B cells has not yet been fully explored. Herein, we sought to address some of these fundamental FL pathogenesis questions through in-depth study of the humoral immune response in mice with *Ezh2* mutant GC B cells.

## RESULTS

### Mutant *Ezh2* provides a fitness advantage to GC B cells

Although $Ezh2^{Y641F}$ induces formation of larger than normal GCs, it is not known whether it confers a selective advantage over WT GC B cells under physiologic conditions in the same microenvironment, which is likely critical for initiating lymphomagenesis. For this we performed mixed chimera bone marrow transplantation experiments using the Cγ1-cre strain (Casola et al., 2006) to drive GC specific expression of $Ezh2^{Y641F}$ from the endogenous *Ezh2* locus (Beguelin et al., 2016) (Figure S1A–S1D). As WT bone marrow donor, we used Cγ1-cre strain carrying $Ptprc^{a}$ (CD45.1), whereas the $Ezh2(Y641F)^{fl/WT}$;Cγ1-cre strain ($Ezh2^{Y641F}$ from hereon) expresses the $Ptprc^{b}$ allele (CD45.2). Cγ1-cre (WT *Ezh2*) bone marrow was mixed with $Ezh2^{Y641F}$ at different ratios and engrafted into *Rag1* KO host mice. Upon engraftment, mice were immunized with the T cell dependent antigen sheep red blood cells (SRBC) to induce GCs, and euthanized at 8 days, when the GC reaction is at its peak (Figure 1A).

Normalizing the percentage of $CD45.1^{+}$ or $CD45.2^{+}$ GC B cells to their respective total B cell populations by flow cytometry (Figure 1B) indicated that mutant *Ezh2* provides a competitive advantage in the GC reaction (Figure 1C), that was even greater when the initial ratio of transplanted cells was skewed towards the WT (Figure 1C). In control experiments, both WT and $Ezh2^{Y641F}$ form GCs (Figure 1C) without altering non-GC B cell ratios (Figure 1D). Confocal microscopy confirmed significantly higher overlap of the GC marker PNA with CD45.2 ($Ezh2^{Y641F}$) than CD45.1 (WT *Ezh2*; Figure 1E and 1F). We also examined early GCs (day 3), and resolving GCs (20 days), and observed similar $Ezh2^{Y641F}$ dominance at both time points (Figure 1G–1J). Hence, mutant *Ezh2* provides a selective advantage to GC B cells throughout the duration of the GC reaction.

Author Manuscript Author Manuscript Author Manuscript Author Manuscript

### Mutant *Ezh2* skews GC polarity to yield expansion of the centrocyte population

Given that EZH2 normally represses cell cycle checkpoint genes to enable DZ proliferation (Beguelin et al., 2013; Beguelin et al., 2017), we predicted that *Ezh2*$^{Y641F}$ competitive advantage likely reflects expansion of the DZ by exaggerating this effect. Yet surprisingly, analysis of splenic GCs showed an increased proportion of centrocytes, shifting the typical DZ:LZ ratio from ~60:30 (Victora et al., 2010) to ~50:40 (Figure 2A–2D). This was further confirmed by confocal microscopy using IgD (B cell follicles), PNA (GC B cells) and CD35 to mark FDCs (a landmark for the LZ niche), revealing clear LZ expansion with increased abundance of GC B cells interdigitated among FDCs (Figures 2E–2G and S2A). We observed a similar effect by crossing *Ezh2*$^{Y641F}$ and Cγ1-cre (WT *Ezh2*) mice with the R26-lox-stop-lox-YFP reporter strain to induce YFP expression in GC B cells (Figures 2H–2J and S2B–S2D). Similar results were observed in lymph nodes of NP-OVA immunized mice (data not shown).

To determine whether *Ezh2*$^{Y641F}$ still disrupts GC polarity when competing with WT *Ezh2* GC B cells in the same microenvironment, we explored DZ/LZ distribution in mixed chimeras (Figure 2K and 2L). This system confirmed significant increase of centrocytes 8 and 20 days after immunization in *Ezh2*$^{Y641F}$, with proportionately fewer centroblasts (Figure 2M). Altogether, these results show that *Ezh2* gain-of-function mutations expand GCs by increasing their centrocyte subpopulation.

### LZ expansion is not due to differentiation blockade

Given that EZH2 inhibitors primarily cause induction of plasma cell differentiation and proliferation arrest in lymphoma cells (Beguelin et al., 2013; Knutson et al., 2012; McCabe et al., 2012b), we reasoned that LZ expansion might reflect impaired GC exit and differentiation. This was tested by immunizing *Ezh2*$^{Y641F}$ or WT mice with NP-OVA (Figure S2E), and measuring secretion of high and low affinity NP-specific immunoglobulins by antibody secreting cells emerging from the GC reaction. Contrary to expectations, *Ezh2*$^{Y641F}$ B cells generated similar frequency of NP$^{+}$ specific IgG1 and IgM splenocytes as compared to WT GC B cells (Figure S2F). NP$^{+}$ specific plasma cells or memory B cell were also generated at similar abundance in *Ezh2*$^{Y641F}$ vs. WT mice (Figure S2G–S2J). *Ezh2*$^{Y641F}$ GC B cells yielded increased, rather than decreased, output of splenic memory B cells (Figure S2K and S2L) as compared to WT controls in the mixed chimera setting. However, the abundance of memory cells was actually proportional to GC B cells (Figure S2M), suggesting that there was no net perturbation in GC exit or terminal differentiation.

We then investigated whether there was any perturbation of fully differentiated, long-lived plasma cells in *Ezh2*$^{Y641F}$ or WT mice (Figure S2N). There was no impairment of IgG1 or IgM secretion from long-lived, high affinity (post-GC) plasma cells (Figure S2O), nor any loss of high-affinity, post-GC plasma cells and long lived plasma cells (Figure S2P and S2Q). There was no reduction in titers or ratios of antigen specific low or high affinity immunoglobulins (Figure S2R and S2S). These results were further confirmed in R26-lox-stop-lox-YFP*;Ezh2*$^{Y641F}$ mice, which manifested a slight increase in post-GC memory B cells and no significant change in plasma cells or plasmablasts in *Ezh2*$^{Y641F}$ mice (Figure

Author Manuscript Author Manuscript Author Manuscript Author Manuscript

S2T–S2W). Taken together, these results show that *Ezh2*$^{Y641F}$ induced expansion of the GC LZ is not explained by differentiation blockade.

### *Ezh2* mutation causes aberrant proliferation of LZ centrocytes

Since LZ expansion by *Ezh2* mutation is not due to differentiation blockade, we next explored if this effect is due to aberrant proliferation. Analysis of splenocytes of mixed chimera mice after immunization with SRBC revealed significant increase in the fraction of Ki67$^{+}$ *Ezh2*$^{Y641F}$ centrocytes (Figure S3A and S3B), with a much smaller effect in centroblasts (Figure S3B).

To more precisely characterize this effect we crossed *Ezh2*$^{Y641F}$ mice with R26-Fucci2aR strain (Mort et al., 2014), encoding reporters that fluoresce red during G1 (mCherry-hCdt1) and green during S/G2/M phases (mVenus-hGem). Flow cytometry revealed that many GC B cells were in S/G2/M phases (mCherry$^{-}$) while naive B cells were in G1/G0 (mCherry$^{+}$mVenus$^{-}$, Figure S3C and S3D). We validated these results by evaluating DNA content in fixed R26-Fucci2aR splenocytes (Figure S3E). We then immunized R26-Fucci2aR;*Ezh2*$^{Y641F}$ and R26-Fucci2aR;C$\gamma$1-cre control mice with SRBC and examined the cell cycle state of GC B cells in spleens 8 days later. We observed a significantly increased S/G2/M and decreased G1 phase GC B cells in R26-Fucci2aR;*Ezh2*$^{Y641F}$, but no cell cycle changes in non-GC B cells (Figure S3F). In normal GC B cells most centrocytes were in G1 (Figure 3A) and centroblasts in S/G2/M phases, as expected (Figure S3G). However, *Ezh2*$^{Y641F}$ mice manifested significant increase in G2/M and reduction in G1 phase centrocytes (Figure 3B and 3C). In contrast there were no differences in the most abundant fractions of centroblasts, (G1 and late M phase, Figure S3G–S3I). Finally, visualization of splenic GCs revealed abundant mVenus$^{+}$ centrocytes enmeshed within the network of FDCs (Figures 3D, 3E and S3J). In contrast *Ezh2* WT GCs, contained much fewer dividing LZ centrocytes and instead the mVenus$^{+}$ signal was mainly present in the DZ.

*Ezh2* mutant centrocytes might also accumulate in the LZ if they did not undergo apoptosis at the same rate as WT cells. To investigate this possibility, we immunized *Ezh2*$^{Y641F}$/WT mixed chimera mice with SRBC and extracted spleens and inguinal and popliteal lymph nodes. We observed significant reduction in the abundance of apoptotic splenic GC B cells in *Ezh2*$^{Y641F}$ mice (Figure S3K and S3L). There was particularly robust reduction of apoptosis in *Ezh2*$^{Y641F}$ centrocytes, and smaller but still significant reduction in *Ezh2*$^{Y641F}$ centroblasts (Figure 3F–3K). Collectively, these data show that *Ezh2* mutation drives GC hyperplasia through enhanced proliferation and survival of centrocytes.

### *Ezh2*$^{Y641F}$ centrocytes fail to re-enter the DZ

The preceding data indicate that *Ezh2*$^{Y641F}$ induces LZ hyperplasia, with proportional increase in plasma and memory cells, but not DZ cells. This was perplexing, since centrocytes typically re-enter the DZ after T cell selection to undergo additional rounds of proliferation and somatic hypermutation (Oprea and Perelson, 1997; Victora et al., 2010) and theoretically should drive proportional increase in centroblasts. Considering that GC B cells are a complex mixture of subpopulations undergoing several transitional phases (Mesin et al., 2016), we performed droplet-based single cell RNA-seq to define how mutant *Ezh2*

Author Manuscript Author Manuscript Author Manuscript Author Manuscript

affects these states. We used the YFP Cre reporter system to avoid sorting based on specific surface markers of pre-defined populations, and isolated $YFP^{+}IgD^{-}$splenocytes (GC B cells and post-GC B cells) from immunized R26-lox-stop-lox-YFP;*Ezh2*$^{Y641F}$ and R26-lox-stop-lox-YFP;Cγ1-cre control mice. Using UMAP we identified two main clusters of cells (Figure S4A and S4B) corresponding to GC B cells and plasma cells (Figure S4C), based on projection of plasma cell signatures and expression of specific genes (Figure S4D). After normalization for total number of analyzed cells, the abundance of plasma cells was slightly increased in *Ezh2*$^{Y641F}$ mice (Figure S4E).

Focusing on the GC B cell population, we next used graph-based clustering and K nearest neighbor analysis to assign cells to clusters with distinct expression profiles, yielding eight discrete clusters of cells (Figure 4A). By projecting GC-associated signatures on to these clusters, we were able to determine that clusters 1 and 2 correspond to centroblasts, clusters 3 and 4 correspond to cells transitioning from DZ to LZ, cluster 5 corresponds to centrocytes, cluster 6 represents putative mature centrocytes transitioning to memory B cells, whereas clusters 7 and 8 manifested the canonical signature of centrocytes that are recycling back to form DZ centroblasts, which typically manifest transient upregulation of *Myc* (Figure 4B). True to their recycling nature, the *Myc* positive cluster created a branch between centroblasts and centrocytes, reflecting the transition of these cells from the LZ to DZ. Projection of genes characteristic of these various subpopulations were accordingly enriched for expression in these respective clusters including *Mki67*, *Ccnb1* and *Ccnb2* for DZ, *Cd83* for LZ, *Myc* for recycling cells, and *Ccr6*, *Cd38* and *S1pr1* for pre-memory and memory cells (Figure 4C).

We then organized the single cell gene expression profiles into a pseudotime vector using the Slingshot algorithm, allowing us to visualize the putative temporal relationships of these various GC B cell subpopulations going from centroblasts to transitional state to centrocyte and branching to either mature centrocyte/pre-memory cells or MYC-activated recycling cells (Figure 4D). After normalizing for cell numbers, this analysis confirmed the relative expansion of centrocytes (36% in *Ezh2*$^{Y641F}$ vs. 28% in WT, Figure 4E). Unexpectedly, we also observed a significant reduction in centrocytes manifesting the MYC-associated recycling signature (3.9% in WT vs. 2.9% in *Ezh2*$^{Y641F}$, Figure 4F), suggesting that *Ezh2*$^{Y641F}$ was impairing recycling to the DZ.

To confirm the reduction in GC recycling cells, we crossed our *Ezh2*$^{Y641F}$ mice with animals bearing GFP-MYC fusion protein expressed from the *Myc* locus (Huang et al., 2008), which allows recycling cells to be identified by flow cytometry (Calado et al., 2012; Dominguez-Sola et al., 2012). Concordant with previous reports (Ersching et al., 2017), $GFP^{+}$ GC B cells were almost exclusively centrocytes (Figure 4G and 4H) and exhibited increased cell size (Figure S4F), consistent with these cells undergoing anabolic growth. GFP-Myc;*Ezh2*$^{Y641F}$ mice exhibited a severe reduction of $GFP^{+}$ GC B cells as compared to GFP-Myc;Cγ1-cre control mice (Figure 4I and 4J), indicating impaired engagement of the MYC program that is required for GC B cells to re-enter the DZ among *Ezh2* mutant centrocytes.

Author Manuscript Author Manuscript Author Manuscript Author Manuscript

### *Ezh2* mutant GC B cells feature transcriptional repression with both gain and spreading of the H3K27me3

The effect of *Ezh2* mutation on the histone landscape has not been evaluated *in vivo* and/or in primary cells. For this we performed liquid chromatography separation and top-down mass spectrometry of histone tryptic peptides extracted from purified GC B cells and naive B cells, to quantify histone modifications in an unbiased manner. We observed a massive increase of H3.1K27me3 in $Ezh2^{Y641F}$ GC B cells, mostly at the expense of reciprocal reduction in H3K27me2 (Figure 5A). Whereas 8% of histone 3.1 was trimethylated in control GC B cells, there was 29.8% trimethylation in *Ezh2* mutant GC B cells. We also observed a smaller but significant reduction in H3K27me1. Surprisingly, the abundance of unmethylated H3K27 was significantly higher in $Ezh2^{Y641F}$ GC B cells (from 31% to 40% of H3.1). This effect although unexpected, is consistent with biochemistry studies showing that $Ezh2^{Y641F}$ exhibits impaired H3K27 monomethylation activity (McCabe et al., 2012a; Ott et al., 2014; Sneeringer et al., 2010; Yap et al., 2011). The minor H3 isoform H3.3 (~15% of H3), which is more dynamic and associated with actively transcribed genes, also showed significant changes although to a lesser degree than H3.1 (Figure S5A). As expected, there were no differences in histone modification profiles between WT and $Ezh2^{Y641F}$ naive B cells (Figure S5B) and virtually no effect on any other histone modification in GC B cells (data not shown).

Given the histone mass spectrometry data, we next examined H3K27me3 genomic distribution in purified centroblasts and centrocytes from three $Ezh2^{Y641F}$ and three WT control mice, using ChIP-Rx (Orlando et al., 2014). Unsupervised analysis revealed profound differences in the H3K27me3 profiles between WT and $Ezh2^{Y641F}$ centroblasts and centrocytes (Figure S5C). Examination of gene promoters revealed that whereas a majority of promoter H3K27me3 peaks (n≈8500) were shared between mutant and WT centroblasts or centrocytes, there was also gain of ~2800 *de novo* promoter peaks in the respective mutant cells, most of which (75%) were present in both centroblasts and centrocytes (Figure 5B). *De novo* H3K27me3 promoters in $Ezh2^{Y641F}$ GC B cells tended to be close to promoters that were marked by H3K27me3 in WT cells (empirical p=0.0012 for centroblasts and p=0.0013 for centrocytes). Notably, we observed spreading of H3K27me3 between WT and *de novo* H3K27me3 peaks in $Ezh2^{Y641F}$ GC B cells (Wilcoxon $p<1x10^{-300}$, Figures 5C and S5D). Hence, *de novo* marked promoters might have become susceptible to gaining H3K27me3 through spreading of the mark from nearby promoters that normally manifest this histone modification.

To link the above ChIP-Rx results to gene transcription we performed RNA-seq in purified centroblasts and centrocytes of $Ezh2^{Y641F}$ and WT control mice. Unsupervised analysis showed a clear segregation of the four GC B cell subsets (Figure S5E). Using a supervised analysis we identified 648 down- and 272 upregulated genes in $Ezh2^{Y641F}$ centroblasts, and 941 down- and 508 upregulated genes in $Ezh2^{Y641F}$ centrocytes (Figure 5D). Centrocyte-repressed genes displayed marked spreading of H3K27me3 both upstream and downstream of well-defined TSS H3K27me3 peaks. Upregulated genes, in contrast, did not contain defined H3K27me3 peaks and had a more modest increase in H3K27me3 surrounding TSSs (Figure 5E). Similar patterns were found in centroblasts (Figure S5F). Moreover, genes

Author Manuscript Author Manuscript Author Manuscript Author Manuscript

linked to both *de novo* (*Ezh2*$^{Y641F}$-specific) and shared H3K27me3 marked promoters, were more repressed in *Ezh2*$^{Y641F}$ GC B cells (FDR<0.005, NES<-1.3 Figure S5G). Hence the *EZH2* mutant transcriptional signature is derived from two sources: further repression of genes already regulated by EZH2 in WT GCs, and *de novo* repression of genes that gain H3K27me3 ectopically in *Ezh2*$^{Y641F}$ GC B cells.

Focusing on centrocytes (the cells most phenotypically perturbed in *Ezh2*$^{Y641}$ mice) and using both hypergeometric and GSEA analyses, we observed that *Ezh2*$^{Y641F}$ downregulated genes were enriched for those that are normally repressed by EZH2 in GC B cells (Beguelin et al., 2013) (Figures 5F and S5H). This is in line with the notion that most gain of H3K27me3 occurs at genes already normally targeted by EZH2 in GC B cells. Consistent with the reduction in MYC-driven GC recycling cells, we observed enrichment for MYC downregulated genes among genes induced in *Ezh2*$^{Y641F}$ centrocytes, and reciprocally, enrichment for MYC upregulated genes being repressed. The GC recycling phase is dependent in part on CD40 signaling, and we observed that genes normally downregulated by CD40 were instead induced in *Ezh2*$^{Y641F}$ centrocytes, suggesting lack of CD40 response. Finally, genes that were significantly repressed in *EZH2* mutant FL patients were also enriched for repression in *Ezh2*$^{Y641F}$ centrocytes (Figures 5F and S5H). Reciprocally, genes that are repressed in *Ezh2*$^{Y641F}$ centrocytes were also repressed in patients with *EZH2* mutant FL (Figure S5I). Low grade FL is mainly composed of malignant centrocyte-like cells, and these data are consistent with these *Ezh2*$^{Y641F}$ centrocytes giving rise to FL.

## Mutant *Ezh2* disrupts dynamic gene expression changes in centrocytes, linked to aberrant H3K27 trimethylation

Phenotypic transitions during the GC reaction are driven by waves of differential gene expression linked to signals received from the microenvironment (Mesin et al., 2016). Many B cell signal responsive genes are repressed in centroblasts but are then induced in centrocytes (Victora et al., 2010). To determine how transcriptional programming is affected in the presence of mutant *Ezh2*, RNA-seq data were used to calculate the trajectory of gene regulation from naive B cells to centroblasts and then centrocytes in *Ezh2*$^{Y641F}$ vs. WT cells. To group genes based on their pattern of perturbation by mutant *Ezh2*, we used K means clustering, which identified eight distinct gene expression modules based on trajectory of the constituent genes across these cell types (Figure 5G and 5H).

Module 1 and 2 genes were aberrantly upregulated in *Ezh2*$^{Y641F}$ centrocytes, albeit with distinct trajectories. These include canonical centrocyte genes; anti-apoptotic factors, and genes involved in antigen presentation (Figure 5G and 5H). Of particular note were genes involved in interaction with FDCs, such as *Tnfrsf13c* (BAFF receptor) (Figure S5J). Module 8 contains genes that are normally downregulated in GC B cells, but are aberrantly upregulated in *Ezh2*$^{Y641F}$ GC B cells. Many of these are normally upregulated when B cells exit the GC reaction and commit to memory B cell differentiation such as *Gpr183*, *Ccr6* and MHC class II antigen presentation genes (Figure S5J). Of note, *Ltb*, which is also involved in interaction with FDCs, was significantly upregulated in Ezh2$^{Y641F}$ centrocytes.

Modules 3, 4, 5, 6 and 7 contain genes that are aberrantly repressed in *Ezh2*$^{Y641F}$ GC B cells, albeit with distinct trajectories (Figure 5G and 5H). Module 3 contains pro-apoptotic

Author Manuscript Author Manuscript Author Manuscript Author Manuscript

BH3 domain genes, and several DZ hallmark genes (Victora et al., 2010). Module 4 contains genes involved in the recycling program of centrocytes re-entering the DZ (Ersching et al., 2017). Of particular interest, modules 5, 6 and 7 contain genes that are normally expressed in the LZ and are linked to Tfh immune synapse signaling but fail to be induced or maintained at their normal levels in the presence of mutant *EZH2*. This includes genes such as *Cd69* (linked to stable Tfh-GC B cell contacts), *Basp1* (induced by B cell activation with anti-IgM and anti-CD40), *Icosl* and *Icam1* (Ise et al., 2018; Liu et al., 2015; Papa and Vinuesa, 2018; Yu et al., 2008; Zaretsky et al., 2017) (Figure S5J).

To determine if the trajectory perturbation of genes was linked to changes in H3K27me3 deposition, we examined their ChIP-seq profiles and observed that all repressed modules exhibited significant gain of H3K27me3, with the exception of module 7, which contains a small fraction of upregulated genes (Figure 5I). In contrast, there was no significant change in H3K27me3 in the upregulated modules (Figure 5I). We performed independent qChIP and qPCR experiments in purified *Ezh2*$^{Y641F}$ and WT B cell subsets to validate these gene expression and H3K27me3 changes for a subset of genes (Figures 5K, 5L, S5K and S5L). In spite of the species difference, genetic heterogeneity and more advanced stage of fully established human FLs, we still observed significant enrichment for repression of cluster 3, 4 and 5 genes, and upregulation of cluster 1 and 8 genes in primary human FLs (Ortega-Molina et al., 2015), with discordance only noted for cluster 7 (Figure 5J). Altogether these results suggest that the primary effect of mutant *Ezh2* is aberrant repression of genes, many of which are normally dynamically regulated during the GC reaction. The fact that many genes linked to Tfh signaling to centrocytes were aberrantly repressed (including the centrocyte recycling program), points to this aspect as a potential driver of early *EZH2* mutant FL pathogenesis.

## *Ezh2*$^{Y641F}$ GC B cells manifest decreased interaction and dependency on Tfh cells

In the GC LZ, B cells require strong interaction with T cells to survive and be selected for their ultimate fate. This normally depends on B cell specificity for antigen (Mesin et al., 2016; Meyer-Hermann et al., 2006; Victora et al., 2010). Yet our data suggest that this process might be impaired in centrocytes bearing the *Ezh2*$^{Y641}$ mutation. To evaluate this possibility, we first assessed the protein levels of adhesion and activation molecules in GC B cells that are involved in the interaction with Tfh cells. SLAM, ICAM-1, ICAM-2 and Ly108 protein expression was significantly downregulated in *Ezh2*$^{Y641F}$ centrocytes (Figure S6A). Next, we assessed whether FACS-sorted *Ezh2* mutant or WT centrocytes (B220$^{+}$CD38$^{-}$Fas$^{+}$CXCR4$^{lo}$CD86$^{hi}$) loaded with OVA antigen could preferentially interact with OVA-primed OT-II Tfh cells (CD4$^{+}$B220$^{-}$PD1$^{hi}$CXCR5$^{hi}$) *ex vivo* (Figure 6A) (Ise et al., 2018) by performing flow cytometry to assess formation of B cell–T cell conjugates by gating on cell duplets, normalizing to cell singlets for quantification (Figure 6B). *Ezh2*$^{Y641F}$ centrocytes formed ~40% less conjugates with Tfh than WT centrocytes (Figure 6C), suggesting that *Ezh2* mutation impairs formation of stable centrocyte-Tfh interactions.

Since T cell help is required for the survival of GC B cells, we hypothesized that *Ezh2* mutant centrocytes must be aberrantly able to survive even without this critical signal. T cell help in the LZ is critically dependent on CD40-CD40L binding between centrocytes and Tfh

Author Manuscript Author Manuscript Author Manuscript Author Manuscript

cells. Blockade of this interaction causes collapse of the GC reaction (Elgueta et al., 2009). To determine if *Ezh2* mutant centrocytes had become less dependent of T cell help, we next immunized $Ezh2^{Y641F}$ and WT mice and then administered two sequential doses of CD40L binding antibody after GCs were already established (Figure 6D). Treatment of WT Cγ1-cre mice with anti CD40L antibody significantly impaired the GC reaction as expected. In striking contrast, there was no significant impairment of GCs in $Ezh2^{Y641F}$ mice (Figure 6E and 6F). To validate these results in a setting where WT and $Ezh2^{Y641F}$ GC B cells must compete within the same microenvironment, we performed mixed chimera experiments (Figure 6G). Examination of spleens and lymph nodes confirmed that there were equal proportions of $Ezh2^{Y641F}$ vs. WT naive B cells (Figure S6B and S6C). As shown earlier, mice immunized with control antibodies display an increased proportion of $Ezh2^{Y641F}$ relative to WT GC B cells. However, upon exposure to CD40L blocking antibodies, this fraction increased even further due to more dramatic loss of WT GC B cells in comparison with $Ezh2^{Y641F}$ GC B cells (Figures 6H, 6I and S6B). We observed similar results with longer duration anti-CD40L treatment (Figure S6D–S6H). As a second approach for interfering with T cell help we performed similar experiments using anti-ICAM-1 blocking antibodies (Figure 6J), which resulted in a further competitive survival advantage of $Ezh2^{Y641F}$ GC B cells (Figures 6K, 6L and S6I–S6K) without changes in naive B cell proportions (Figure S6L).

## $Ezh2^{Y641F}$ GC B cells evade Tfh directed clonal selection and affinity maturation to dominate the GC reaction

T cell help is required for centrocytes to recycle back to the DZ for additional mutagenesis and hence directs clonal evolution of the immunoglobulin loci (Mesin et al., 2016). Although our above data suggest that the dominant effect of mutant *Ezh2* is to disrupt this process, definitive genetic proof requires in-depth analysis of clonal diversification during the GC reaction. Using immunized R26-lox-stop-lox-YFP;$Ezh2^{Y641F}$ and R26-lox-stop-lox-YFP;Cγ1-cre control mice we excised individual $YFP^+$ GCs by microdissection, and performed single cell genomic clonality assays by sequencing IgM and IgG1 variable regions (Figure S7A). Individual variable regions sequences from $Ezh2^{Y641F}$ GCs were significantly more likely to be classified as centrocytes (40% of sequences) compared to those from WT GCs (23%; chi-squared $p<0.001$), as expected given the expansion of LZ phenotype in $Ezh2^{Y641F}$ GCs. The mean mutation frequency of WT GC B cells was significantly higher than that of $Ezh2^{Y641F}$ GC B cells (Wilcoxon rank-sum test $p<1x10^{-5}$; means=0.016/bp, 0.011/bp, respectively). Further, the mutation frequency of WT centroblasts was significantly higher than WT centrocytes ($p=0.005$, Figure 7A), consistent with centroblasts representing the progeny of centrocytes that recycle back to the DZ. In contrast, centroblasts did not exhibit any increase in mutation frequency as compared to centrocytes in $Ezh2^{Y641F}$ mutant mice (Figure 7A), supporting that after their initial transit through the DZ, $Ezh2^{Y641F}$ centrocytes are less likely to recycle back to the DZ for additional mutagenesis.

We found multiple pieces of evidence consistent with disrupted affinity maturation in $Ezh2^{Y641F}$ mice. We observed significantly reduced diversity of clones among $Ezh2^{Y641F}$ GC B cells as compared to WT GCs based on the distribution of clone sizes (Figure 7B). We

Author Manuscript Author Manuscript Author Manuscript Author Manuscript

also observed differences among B cell lineage trees taken from *Ezh2*$^{Y641F}$ and WT mice. During normal affinity maturation, a combination of selection and genetic drift produces shared mutations among sequences within a clone, forming the internal branches of its lineage tree. Mutations shared by all sequences form the “trunk” branch leading immediately from the germline to the sequences’ universal common ancestor. Lineage trees estimated from *Ezh2*$^{Y641F}$ mice had proportionally shorter trunks and internal branches compared to lineage trees estimated from WT mice (Figure 7C and 7D). *Ezh2*$^{Y641F}$ trees were more star-like, with external branches radiating out from a single common ancestor closely related to their germline sequences (e.g. Figure 7C). *Ezh2*$^{Y641F}$ mice showed evidence of reduced efficacy of affinity maturation. Immunization with NP-OVA is characterized by a tryptophan to leucine substitution at IMGT codon position 38 of the V gene V1–72*01 that strongly increases binding affinity to NP-OVA (Rajewsky et al., 1987). Of the 46 V1–72*01-derived sequences observed in WT GCs, five sequences from three clones in two mice contained leucine at this position. By contrast, none of the 66 V1–72*01-derived sequences from *Ezh2*$^{Y641F}$ mice contained this substitution.

As further confirmation that *Ezh2*$^{Y641F}$ GCs have decreased clonal diversity, we generated *Ezh2*$^{Y641F}$ mice that were also homozygous for R26R-Confetti allele (Livet et al., 2007), which labels cells in up to 10 different color combinations when activated (Figure S7B). Confocal microscopic examination of GCs from immunized R26R-Confetti mice showed that *Ezh2*$^{Y641F}$ displayed reduced color diversification compared to those of Cγ1-cre mice (Figures 7E and S7C). To assess this from a quantitative standpoint we generated an optimal segmentation algorithm that classified cells within GCs according to color combination (Figure S7D and S7E). Quantifying the abundance of cells per clone within GCs revealed a significant reduction in the Shannon entropy (diversity) among individual *Ezh2*$^{Y641F}$ GCs, as well as when all the tested GCs were combined per mouse (Figure 7F–7H). To confirm this pattern at the sequence level, we performed single cell V region sequencing from individual GCs as above, and grouped sequences into clonal clusters based on their sequence similarity. Confirming our data from the YFP system, R26R-Confetti*;Ezh2*$^{Y641F}$ mice had reduced clonal diversity (Figure 7I), and their lineage trees had reduced proportional trunk and internal branch lengths (Figure 7J). To assess the reliability of clonal diversity measures obtained in our confocal microscopy analysis, we observed that while color combinations do not completely distinguish sequence-defined clonal clusters, sequences within clones were enriched for particular combinations of colors (Figure S7F). This pattern may be due to persistent recombination of the Cγ1-cre cassette.

Taken together, these results confirm that *Ezh2* mutant GCs fail to engage T cells, and hence do not receive Tfh signals that would induce recycling to the DZ. In contrast to normal cells, which cannot survive without T cell help, *Ezh2* mutant centrocytes can further proliferate in the LZ. Hence the dominant competitive advantage effect of the *Ezh2* mutation during early stages of transformation is to uncouple GC B cells from the critical T cell help checkpoint, which allows waves of GC B cells entering the LZ to persist and expand regardless of their immunoglobulin status.

Author Manuscript Author Manuscript Author Manuscript Author Manuscript

### *Ezh2*$^{Y641F}$ GC B cells switch from T cell to FDC dependency

Given that *Ezh2*$^{Y641F}$ GC B cells were less dependent on T cell help, we postulated that they might be instead dependent on FDCs, especially given the expanded FDC networks and upregulation of genes linked to FDC signaling. Maintenance of FDC networks and GCs requires signaling through lymphotoxin b (Ngo et al., 1999), which is expressed on GC B cells and was further induced in *Ezh2* mutant centrocytes (Figure 5K). To determine whether *Ezh2* mutant GCs were dependent on these FDC interactions we administered soluble lymphotoxin β receptor (mLTβR) (Browning et al., 1995) to immunized mixed chimera mice to suppress FDC functions (Figure 8A). As expected, exposure to this inhibitor caused a modest overall reduction in splenic B cells, and a more severe reduction in the abundance of GC B cells (Figure 8B and 8C). However, in contrast to their marked advantage in the setting of Tfh interaction blockade, *Ezh2*$^{Y641F}$ GC B cells manifested loss of competitive fitness and appeared even more sensitive to FDC blockade than their WT counterparts when exposed to mLTβR (Figure 8D and 8E). As expected there was no selective effect of mLTβR against *Ezh2*$^{Y641F}$ or WT naive B cells (Figure 8F).

These data suggest that *Ezh2* mutation reprograms the GC immune niche to generate an abnormal tissue featuring FDC dependent-expansion of aberrant centrocytes. To determine if this pattern is reflected in primary human FLs with *EZH2* mutations we performed immunohistochemistry staining for CD21/CD35 on a tissue microarray with 209 genetically characterized FL patients, of which 17.2% carried *EZH2*$^{Y641}$ point mutations (Kridel et al., 2016). There was no significant association between *EZH2* mutation status and histological grade. Focusing on the grade 1 and 2 FLs, we found that *EZH2*$^{Y641}$ FLs feature significantly greater association with intact and extensive FDC networks as compared to *EZH2* WT lymphomas, regardless of grade (Figure 8G), and exemplified in Figure 8H. Staining for CD4 and CD8 T cells did not reveal significant differences in abundance of these cells among *EZH2* mutant and WT FLs (data not shown). Collectively these data provide an explanation for how FLs arise from aberrant GC reactions directed by mutant *EZH2* reprogramming of the immune microenvironment.

## DISCUSSION

Our study demonstrates that *Ezh2* mutation sets the stage for FL pathogenesis in GC B cells by remodeling dynamic interactions between B cells, Tfh cells and FDCs. This likely occurs primarily due to loss of plasticity of transcriptional programming in centrocytes, which normally respond rapidly to external signals that direct them to alternative cell fates (Shlomchik et al., 2019). One of our central findings is that *Ezh2* mutant GC B cells manifest reduced dependency on LZ T cell help, suggesting that they no longer need to compete for access to T cell help, allowing the massive numbers of B cells arriving in the LZ to survive and persist as slowly proliferative centrocytes.

Lack of T cell help normally results in death of centrocytes (Mayer et al., 2017; Stewart et al., 2018). The lower apoptosis rate in the *Ezh2*$^{Y641F}$ LZ vs. DZ may be explained by the observation that LZ GC B cells mainly die by default if they are not positively selected (Stewart et al., 2018). The survival and proliferation phenotype of *Ezh2* mutant centrocytes is largely explained through their driving expansion of and dependency on FDCs. Given that

Author Manuscript Author Manuscript Author Manuscript Author Manuscript

centrocytes normally recycle to the proliferative DZ, it is hard to imagine how FLs could form, since LZ B cells should be quickly overwhelmed by rapidly proliferating centroblastic cells. We provide evidence for how this situation might arise: since mutant *Ezh2* impairs interaction with Tfh cells, centrocytes would not receive signals that trigger the MYC-dependent GC recycling response. The relevance of these findings to FL is further suggested by strong association between *EZH2* mutation with dense FDC networks, and persistence of the *Ezh2* mutant centrocyte transcriptional program.

From the mechanistic perspective, in the normal GC reaction EZH2 mediates establishment of bivalent chromatin at promoters that are repressed in the DZ and re-activated in the LZ (Beguelin et al., 2013). Mutation of *Ezh2* at Y641 disrupts this transcriptional plasticity. Indeed, a dominant effect of mutant *Ezh2* was to prevent induction of genes that are normally upregulated in centrocytes, associated with spreading of H3K27me3 mark from gene promoters to neighboring chromatin. This is consistent with the fact that WT EZH2 has poor trimethylation activity (McCabe et al., 2012a; Sneeringer et al., 2010; Yap et al., 2011) and can therefore only generate H3K27me3 where its binding is most stable (e.g. around promoters (Laugesen et al., 2019)). In the case of the $EZH2^{Y641}$ mutant, it is likely that its more transient presence at surrounding sites is sufficient to generate H3K27me3 from pre-existing H3K27me2. Interestingly, the H3K27me2 mark has been proposed to stabilize transcriptional programs by preventing ectopic firing of promoter and enhancers (Conway et al., 2015; Ferrari et al., 2014; Lee et al., 2015). However in the presence of mutant EZH2, H3K27me2 marked promoters may become more likely to acquire H3K27me3. More efficient spreading of PRC2 to these sites may be further favored through the EED subunit, which stabilizes PRC2 binding through its association with H3K27me3 (Hansen et al., 2008; Margueron et al., 2009; Oksuz et al., 2018). Another relevant consideration that might explain preferential spreading of H3K27me3 to nearby promoters, could be their shared localization within topologically associating domains (TAD) (Donaldson-Collier et al., 2019). Finally, in contrast to the profiles of B lineage splenocytes expressing $Ezh2^{Y641F}$ (Souroullas et al., 2016), we could not link transcriptional upregulation in centrocytes with loss of H3K27me3. Hence we favor the view that in the GC context, upregulated genes are associated with indirect effects of $Ezh2^{Y641F}$, such as aberrant downregulation of transcriptional repressors or alteration of signaling pathways.

Collectively, these data suggest that *EZH2* mutation favors malignant transformation through reprogramming of the immune niche. *EZH2* mutations tend to occur early during transformation (Chapuy et al., 2018; Green, 2018), suggesting that in contrast to solid tumors where loss of immune signaling tends to be a late occurrence, remodeling of the immune response might be critical for initiation of GC derived lymphomas. Along these lines, it is notable that GC B cells already normally manifest many of the hallmarks of tumor cells (e.g. tolerance of genomic instability, unrestrained proliferation, etc., (Mlynarczyk et al., 2019). Abnormal outgrowth of GC B cells is restricted by their need for T cell help. Hence there is logic to the notion that founder mutations in GC derived lymphomas would have the effect of overcoming this mechanism. EZH2 inhibitors are highly active against *EZH2* mutant FLs. It is intriguing to speculate that this may be due at least in part to restoration of proper interactions between FL centrocytes with their immune microenvironment.

Author Manuscript Author Manuscript Author Manuscript Author Manuscript

# STAR METHODS

## LEAD CONTACT AND MATERIALS AVAILABILITY

Further information and requests for resources and reagents should be directed to and will be fulfilled by the Lead Contact, Ari M. Melnick (amm2014@med.cornell.edu). This study did not generate new unique reagents.

## EXPERIMENTAL MODEL AND SUBJECT DETAILS

**Mouse models—**Animal care was in strict compliance with institutional guidelines established by the Weill Cornell Medical College, the Guide for the Care and Use of Laboratory Animals (National Academy of Sciences 1996), and the Association for Assessment and Accreditation of Laboratory Animal Care International. Conditional *Ezh2(Y641F)*$^{fl}$ knock-in model was generated in our lab (Beguelin et al., 2016). By crossing *Ezh2(Y641F)*$^{fl}$ with the transgenic Cγ1-cre strain (The Jackson Laboratory, stock 010611) we generated heterozygous mice. As control group, we used *EZH2(Y641F)*$^{WT}$ Cγ1-cre positive littermates. The following strains were obtained from Jackson Laboratory: C57Bl/6J (CD45.2, stock 000664), B6.SJL-*Ptprc*$^{a}$ *Pepc*$^{b}$/Boy (CD45.1, stock 002014), *Rag1* KO (stock 002216), R26-lox-stop-lox-YFP (stock 006148), OT-II (stock 004194), R26R-Confetti (stock 013731), GFP-Myc (stock 021935). R26-Fucci2aR was developed by J. Jackson group (Mort et al., 2014).

## METHOD DETAILS

**Germinal center assessment in mice—**The Research Animal Resource Center of the Weill Cornell Medical College of Medicine approved all mouse procedures. All knockout, knock-in and transgenic mice were used for assessment of the GC formation. Age- and sex-matched mice were immunized intraperitoneally at 8 to 12 weeks of age with either 0.5 ml of a 2% sheep red blood cell (SRBC) suspension in PBS (Cocalico Biologicals), or 50 μg of the highly substituted hapten NP ($NP_{16}$ to $NP_{32}$) conjugated to the carrier protein ovalbumin (OVA, Biosearch Technologies), or CGG (Chicken Gamma Globulin, Biosearch Technologies), or KLH (Keyhole Limpet Hemocyanin, Biosearch Technologies) absorbed to aluminum hydroxide (alum, ThermoFisher Scientific) at a 2:1 ratio. To induce GC reaction in popliteal and inguinal lymph nodes, mice were injected subcutaneously in footpads with 25 μg $NP_{16}$-OVA. In the experiments where interactions with Tfh or FDC were blocked *in vivo*, mice received 100 μg anti CD40L antibody i.v. (clone MR-1, BioXCell BE0017), 150 μg anti ICAM-1 antibody i.p. (clone YN1/1.7.4, BioXCell BE0020), 100 μg recombinant mLTβR (a fusion protein of lymphotoxin β receptor and Fc region of mouse IgG, which acts as inhibitor of transmembrane LTβR) i.v. (R&D Systems 1008-LR), or control IgG antibodies (BioXCell BE0091 and BE0090).

**Chimeric bone marrow transplantations—**Bone marrow cells were harvested from 8–12 week old Cγ1-cre CD45.1 and *Ezh2(Y641F)*$^{fl/WT}$;Cγ1-cre CD45.2 mice. WT and *Ezh2*$^{Y641F}$ bone marrow cells were mixed at the indicated ratios and one million cells were injected into the tail veins of sub-lethally irradiated (650 rads) $Rag1^{-/-}$ host females. One month after transplant to ensure engraftment, mice were immunized and treated as indicated in the figures.

Author Manuscript Author Manuscript Author Manuscript Author Manuscript

**Flow cytometry analysis and cell sorting—**Single-cell suspensions from mouse spleens, lymph nodes and bone marrow were incubated with Fc block antibody (CD16/CD32, BD 553142) and subsequently stained using the following fluorescent-labeled anti-mouse antibodies: from eBioscience, ThermoFisher Scientific: eFluor506 anti-B220 (69–0452, dilution 1:750), APC anti-CD38 (17–0381, dilution 1:750), PE anti-CXCR4 (12–9991, dilution 1:400), APC anti-CD4 (17–0041, dilution 1:750), PerCP-Cy5.5 anti-CD45.1 (45–0453, dilution 1:750), PE-Cy7 anti-CD45.2 (25–0454, dilution 1:750), FITC anti-PD-1 (11–9985, dilution 1:200), PE-Cy7 streptavidin (25–4317, dilution 1:1000); from BD Biosciences: APC and BV786 anti-B220 (553092 and 563894, dilution 1:750), PE, PE-Cy7 and BV421 anti-FAS (554258, 557653 and 562633, dilution 1:750), FITC and BV395 anti-CD38 (558813 and 740245, dilution 1:750), PE-Cy7 and BV421 anti-CD86 (560582 and 564198, dilution 1:500), biotin anti-CXCR4 (551968, dilution 1:400), biotin anti-CXCR5 (551960, dilution 1:400), PE and BV510 anti-IgD (558597 and 563110, dilution 1:750), APC and BV421 anti-IgG1 (560089 and 562580, dilution 1:500), BUV737 anti-CD138 (564430, dilution 1:500), AF647 anti-cleaved caspase-3 (560626, dilution 1:100), BV421 anti-Ki67 (562899, dilution 1:500), BUV395 anti-BAFF-R (742871, dilution 1:400), BV650 anti-ICAM-2 (740470, dilution 1:300), BV711 anti-Ly108 (740823, dilution 1:300), AF488 anti-EZH2 (562479, dilution 1:50); from BioLegend: APC-Cy7 and PE anti-B220 (103224 and 103208, dilution 1:750), APC-Cy7 anti-CD38 (102728, dilution 1:750), PerCP-Cy5.5 anti-GL7 (144610, dilution 1:750), PerCP-Cy5.5 anti-FAS (152610, dilution 1:500), APC anti-CD86 (105012, dilution 1:500), biotin anti-CD83 (121504, dilution 1:400), PE-Cy7 and BV421 anti-CD138 (142514 and 142508, dilution 1:500), APC-Cy7 anti-CD45.2 (109824, dilution 1:750), APC streptavidin (405207, dilution 1:1000), PerCP-Cy5.5 anti-ICAM-1 (116123, dilution 1:300); from Biosearch Technologies: PE NP (N-5070–1, dilution 1:500); from Cell Signaling: AF647 anti-H3K27me3 (12158, dilution 1:400). NIP-haptenated FITC was obtained from M. Shlomchik lab (Anderson et al., 2007). DAPI was used for the exclusion of dead cells. For internal markers, cells were fixed and permeabilized with BD Cytofix/Cytoperm Fixation/Permeabilization Solution Kit (BD Biosciences) and further permeabilized with cold Phosflow Perm Buffer III (BD Biosciences). APC conjugated Annexin V (BD Biosciences 550475, dilution 1:100) in Annexin V binding buffer (BD Biosciences) was used to identify apoptotic cells. FITC-VAD-FMK pan-caspase inhibitor (BioVision) was used as a marker for detection of activated caspase in apoptotic cells. Data were acquired on BD FACS Canto II and BD Fortessa flow cytometer analyzers, and analyzed using FlowJo software package (Becton Dickinson). When B cell populations were sorted, single-cell suspensions of splenocytes were pre-enriched in B cells using CD45R (B220) magnetic microbeads (Miltenyi Biotec, 130–049-501). Cell sorting was performed using BD Aria II sorter with 5 lasers (355, 405, 488, 561, 640), and BD Influx sorter with 6 lasers (355, 405, 445, 488, 561, 640).

**Tfh-centrocyte interaction *ex vivo*—**Conjugate formation assays were performed as previously described (Ise et al., 2018). Sorted splenic centrocytes ($B220^{+}CD38^{-}Fas^{+}CXCR4^{lo}CD86^{hi}$) from NP-CGG immunized Cγ1-cre mice were incubated with Fc block and then stained with 1 μM cell tracer CFSE (Life Technologies) and *Ezh2*$^{Y641F}$ centrocytes with 1 μM cell tracer Violet (Life Technologies). After washing with PBS, centrocytes were incubated with 5 μM OVA323–339 (MBL International, TS-M703) for 2 hours at 37°C. Ten

Author Manuscript Author Manuscript Author Manuscript Author Manuscript

thousand centrocytes (10,000 WT or 5,000 WT + 5,000 *Ezh2*$^{Y641F}$) were mixed with 5,000 splenic Tfh (CD4$^{+}$B220$^{-}$PD1$^{hi}$CXCR5$^{hi}$) sorted from OVA immunized OT-II mice, and cultured in 96-well U-bottom plates for 45 minutes at 37°C. Cells were next stained with anti-B220 (PE) and anti-CD4 (APC). Cells were vigorously pipetted to disrupt nonspecific conjugates and CD4 expression on B220$^{+}$ cells was analyzed by flow cytometry.

**Immunofluorescence and imaging of tissues—**Spleens and lymph nodes were fixed in 4% paraformaldehyde and either embedded in 2% low melt agarose for vibrotome sectioning, or subjected to sucrose gradient of 10%, 20% and 30%, embedded in O.C.T. and frozen down for cryostat sectioning. Mouse models coding for fluorescent proteins (R26-lox-stop-lox-YFP, R26R-Confetti and R26-Fucci2aR) were injected with 2 μg BV421-conjugated anti-CD35 (BD Biosciences 740029) when indicated 16 hours before euthanizing, and tissues were sectioned using a vibratome (70 μm for imaging and 150 μm when single GCs were aisolated). For quantification of chimeras (Figure 1) and LZ staining (Figure 2E), frozen tissues in O.C.T. were sectioned using a cryostat (7 μm), incubated with biotinylated Peanut Agglutinin (PNA, Vector Laboratories B-1075, dilution 1:500) followed by streptavidin conjugated to AF488 (BioLegend, 405235, dilution 1:500) or AF555 (Invitrogen, S32355, dilution 1:500), and the following fluorochrome-conjugated antibodies: AF594 anti-CD45.1, AF647 anti-CD45.2, AF488 anti-IgD (BioLegend 110750, 109817, 405717, dilution 1:200). Tissue sections were imaged at 40x or 25x using a Zeiss LSM 880 confocal microscope with 7 laser excitations at 405, 458, 488, 514, 561, 594 and 633, and analyzed using Fiji (ImageJ) software (Schindelin et al., 2012).

**Immunohistochemistry and FDC pattern in TMAs—**For immunohistochemical staining of CD21/CD35 (antibody clone 2G9, Cell Marque), 4 μm slides of the tissue microarrays of 232 primary diagnosed FL cases, which were previously published (Kridel et al., 2016), were used and 209 cases were available for FDC evaluation. 155 cases were grade 1 or 2; 35 were grade 3, and there was not significant correlation of FL grade with the presence of *EZH2* mutation (Fisher's exact test, p=0.209). Staining was performed on a Benchmark XT platform (Ventana). FDC network pattern was classified by a board certified pathologists as (1) dense: almost all tumor follicles were packed by FDC, (2) disrupted: scattered or peripheral presence of FDC, (3) absence.

**ELISPOT—**Splenocytes were harvested 12 days after NP-OVA immunization, and bone marrow 76 days after NP-KLH immunization. Secreted NP-specific immunoglobulin IgG1 and IgM levels from one million cells per well of 96-well plate were tested for binding to $NP_4$- and $NP_{30}$-BSA (Biosearch Technologies, N-5050H and N-5050XL) coated plates by enzyme-linked immune absorbent spot (ELISPOT). HRP-conjugated antibodies anti-IgG1 and anti-IgM were obtained from SouthernBiotech (1070–05 and 1020–05).

**ELISA—**Murine serum samples were collected before immunization, 12 days after NP-OVA, and 22 and 76 days after NP-KLH immunization, and immunoglobulin levels were analyzed by ELISA. Sera were tested for the binding of NP-specific IgG1, IgG2a, IgG2b, IgG3, IgA, IgM, Igκ and Igλ antibodies (SouthernBiotech, 5300–01, 1050–01 and 1060–01) to $NP_4$-and $NP_{30}$-BSA coated plates.

Author Manuscript Author Manuscript Author Manuscript Author Manuscript

**Single cell RNA-seq and analysis—**$YFP^{+}IgD^{-}$ splenocytes were sorted from 3 R26-lox-stop-lox-YFP;Cγ1-cre and 3 R26-lox-stop-lox-YFP;*Ezh2(Y641F)*$^{fl/WT}$;Cγ1-cre mice 8 days after SRBC immunization. Ten thousand sorted cells from each spleen were subjected to single cell RNA-seq using 10X Genomics Chromium platform. Library preparation for single cell 3' RNA-seq v2, sequencing and post-processing of the raw data was performed at the Epigenomics Core at Weill Cornell Medicine. Libraries were prepared according to 10X Genomics specifications. Briefly, the six independent cellular suspensions were loaded onto the 10X Genomics Chromium platform to generate barcoded single-cell GEMs (Gel Bead-In Emulsions). After RT reaction, GEMs were broken and the single-strand cDNA was cleaned up with DynaBeads MyOne Silane Beads (ThermoFisher Scientific). cDNA was amplified for 12 cycles. Quality of the cDNA was assessed using an Agilent Technologies 2100 Bioanalyzer, obtaining a product of about 1588 bp. This cDNA was enzymatically fragmented, end repaired, A-tailed, subjected to a double-sided size selection with SPRIselect beads (Beckman Coulter) and ligated to adaptors provided in the kit. A unique sample index for each library was introduced through 14 cycles of PCR amplification. Indexed libraries were subjected to a second double-sided size selection, and libraries were then quantified using Qubit fluorometric quantification (ThermoFisher Scientific). The quality was assessed on an Agilent Technologies 2100 Bioanalyzer, obtaining an average library size of 437 bp. Libraries were diluted to 10 nM and clustered on a HiSeq4000 at 1 nM on a pair end read flow cell and sequenced for 26 cycles on R1 (10x barcode and the UMIs), followed by 8 cycles of I7 Index (sample Index), and 98 bases on R2 (transcript). Primary processing of sequencing images was done using Illumina's Real Time Analysis software (RTA). 10x Genomics Cell Ranger Single Cell Software suite v3.0.2 (https://support.10xgenomics.com/single-cell-gene-expression/software/pipelines/latest/what-is-cell-ranger) was used to perform sample de-multiplexing, alignment (mm10), filtering, UMI counting, single-cell 3'end gene counting and performing quality control using the manufacturer parameters.

Libraries were sequenced to an average of 250 million reads per sample with average of 2,853 cells per sample and an average depth of 100 thousand reads per cell (resulting in 77% average sequencing saturation). Sequencing captured 14,625 mean genes per library, 1,448 median genes per cell and 3,654 median unique molecular identifiers (UMIs) per cell (Figure S4A and Table S1). Seurat package was used to identify genes and cells suitable for inclusion in the analysis and to identify the most variable genes (Stuart et al., 2019). Only genes that were present in at least 10 cells, and cells that had at least 500 and at most 5000 unique genes expressed, and mitochondrial gene expression fraction less than 5%, were considered for the analysis (Figure S4A and Table S1). Most variable 3,000 genes were identified using variance stabilizing transform in Seurat. Cells were clustered using graph-based clustering on the first 30 principal components with a resolution of 0.5. Dimensionality reduction was performed using UMAP on the network using 15 nearest neighbors on normalized gene expression values (n=10,334 cells *Ezh2*$^{Y641F}$ and 6,782 WT cells). Principal pseudotime was calculated using Slingshot and dyno package (Saelens et al., 2019; Street et al., 2018). Scores for pathways related gene sets were projected onto cells by taking the z-score of each gene and summing them (Hanzelmann et al., 2013; Lee et al., 2008). In the case where both up- and downregulated genes were reported for a pathway

Author Manuscript Author Manuscript Author Manuscript Author Manuscript

both signatures were merged by summing the normalized upregulation score and the downregulation score together. For pathways gene signatures from MSigDB and as well as manually defined gene sets from literature were used (Liberzon et al., 2011). Using this procedure the clusters that correspond to plasmablasts were identified and removed for the secondary analysis. After removing plasmablasts the most variable genes were recalculated and the above protocol was repeated using only the GC B cells.

**Bulk RNA-seq and analysis—**Naive B cells ($B220^+CD38^+Fas^-IgD^+$), centroblasts ($B220^+CD38^-Fas^+CXCR4^{hi}CD86^{lo}$) and centrocytes ($B220^+CD38^-Fas^+CXCR4^{lo}CD86^{hi}$) were sorted from spleens of 4 Cγ1-cre and 4 *Ezh2(Y641F)*$^{fl/WT}$;Cγ1-cre mice 8 days after SRBC immunization. A minimum of fifty thousand and maximum of one hundred thousand cell type per spleen were collected into Trizol reagent (Invitrogen). RNA was extracted following the manufacturer instructions and RNA quality was evaluated using Agilent Technologies 2100 Bioanalyzer. Library preparation, sequencing and post-processing of the raw data was performed at the Epigenomics Core at Weill Cornell Medicine. Samples that passed the quality control (RNA Integrity Number ≥8) were subjected to library preparation using the Illumina TruSeq RNA sample kits, according to the manufacturer. Briefly, poly A+ RNA was purified from 100 ng of total RNA with oligo-dT beads. Purified mRNA was fragmented with divalent cations at elevated temperature, to ~200 bp. Following dscDNA synthesis, the double stranded products are end repaired, followed by addition of a single 'A' base and then ligation of the Illumina TruSeq adaptors. The resulting product was amplified with 15 cycles of PCR. Libraries were validated using the Agilent Technologies 2100 Bioanalyzer and Quant-iT™ dsDNA H S Assay (Life Technologies). Each library was made with a unique Index sequence and libraries were pooled for sequencing. The pool was clustered at 6.5 pM on a single end read flow cell and sequenced for 50 cycles on an Illumina HiSeq 2500 to obtain ~80 million reads per sample. Primary processing of sequencing images was done using Illumina's Real Time Analysis software (RTA) as suggested by Illumina. CASAVA 1.8.2 software was used to perform image capture, base calling, demultiplexing samples and generation of raw reads and respective quality scores. Adapter removal was performed using cutadapt and Trim Galore! (v0.4.1; www.bioinformatics.babraham.ac.uk/projects/trim_galore/). Reads were aligned with STAR transcriptome aligner (v2.5.1b, (Dobin et al., 2013) using two-pass alignment to mm10 genome and Gencode M12 gene reference (Frankish et al., 2019). Reads quantification was performed using subread featureCounts (Liao et al., 2014). Differential gene expression analysis was performed using DESeq2 on gene counts (Love et al., 2014) comparing the mutant to WT in centroblasts and centrocytes. Genes with fold-change>1.5 and $p<0.01$ after adjusting for multiple testing using Benjamini-Hochberg correction were taken as differentially expressed (Benjamini and Hochberg, 1995). See Table S2 for differentially expressed genes. For normalized expression, gene counts were normalized using TMM (Robinson and Oshlack, 2010). A similar approach was taken to compare each of WT and mutant samples in centroblasts and centrocytes to WT naive B cells. Clustering to define modules was performed on standardized log2 fold-change values relative to naive B cells using fuzzy c-means clustering with 8 clusters and fuzzifier parameter as selected by Schwämmle-Jensen method (Schwammle and Jensen, 2010). See Table S2 for gene lists within each module. Gene Set Enrichment Analysis (GSEA) was performed using fgsea by

Author Manuscript Author Manuscript Author Manuscript Author Manuscript

ranking the genes on the resulting log2 fold-change statistic from DESeq2 and calculating enrichment on the Molecular Signatures Database (MSigDB) entries (Liberzon et al., 2011; Subramanian et al., 2005). Pathway analysis was performed using PAGE algorithm (Goodarzi et al., 2009). See Table S3 for gene lists within each pathway.

**ChIP-seq and analysis—**Between 50,000 and 100,000 centroblasts ($B220^{+}CD38^{-}Fas^{+}CXCR4^{hi}CD86^{lo}$) and centrocytes ($B220^{+}CD38^{-}Fas^{+}CXCR4^{lo}CD86^{hi}$) were sorted from spleens of 3 Cγ1-cre and 3 *Ezh2(Y641F)*$^{fl/WT}$;Cγ1-cre mice 8 days after SRBC immunization. Cells were fixed with 1% formaldehyde and cell pellets were snap frozen in liquid nitrogen. MicroChIP was performed using TrueMicroChip kit (Diagenode) according to manufacturer instructions with following modifications. For each replicate, ~20,000 cells were pooled together with 1 million Drosophila Kc167 cells in 1 ml total volume and processed using Covaris E220E sonicator at peak power 140, duty factor 5, 5 cycles/burst, 20 minutes per sample. The sonicated samples were then cleared by 10 minutes centrifugation and mixed with 20 μg antibody (anti-H3K27me3, Cell Signaling 9733), and incubated overnight with rotation at 4°C. Complexes were pulled down using Protein A Dynabeads (ThermoFisher Scientific), washed and de-crosslinked with kit buffers, and DNA was isolated using standard phenol-chloroform procedure. Libraries were prepared using MicroPlex Library preparation kit (Diagenode), with 8 cycles of amplification, and cleaned up using AMPureXP beads (Beckman Coulter). Libraries were validated using Agilent High Sensitivity D1000 ScreenTape and pooled for sequencing using Illumina NextSeq 500, 1x75 bp (Rockefeller University Genomics Resource Center). Resulting .fastq files were aligned to mouse mm10 and Drosophila dm6 genomes using bwa-mem function of the BWA suite. ChIPseq data was normalized to dm6 spike-in reads using CompChIPseq algorithm, an analysis approach developed by (Blanco et al., 2019), which performs local cyclic Loess regression of spike-in reads to accurately normalize ChIP-seq data in a genome-wide manner. Read density heat maps were generated using DeepTools suite (Ramirez et al., 2014). Log2 ratios were calculated using normalize read counts in promoter regions (TSS +/-5kb) and plotted using denstrip R package with gamma value=4 (Jackson, 2008). ChIPseq peaks were called using the SICER algorithm (Xu et al., 2014) on pooled BAM files from all respective replicates (fold-change>2, $q<0.01$). See Table S4 for ChIP-seq peaks location. To determine the distance between *de novo* H3K27me3 promoters and the rest of H3K27me3 marked promoters, for each *Ezh2*$^{Y641F}$ *de novo* H3K27me3-occupied TSS, the genomic distance to the nearest H3K27me3-occupied TSS was computed. The genomic distance between all RefSeq TSS was then computed. To test if the median distance between H3K27me3 TSS was shorter than expected given the distances between TSSs, we randomly sampled, without replacement, n=1000 sets of TSS with the same size as *Ezh2*$^{Y641F}$ *de novo* H3K27me3-occupied TSS and computed the median distance between TSS for each set. The proportion of these median distances that exceeded the median distance between H3K27me3-occupied TSS was used to determine the empirical p-value.

**qChIP—**Between 50,000 and 100,000 centrocytes ($B220^{+}CD38^{-}Fas^{+}CXCR4^{lo}CD86^{hi}$) were sorted from spleens of 3 Cγ1-cre and 3 *Ezh2(Y641F)*$^{fl/WT}$;Cγ1-cre mice 8 days after SRBC immunization. Cells were subjected to H3K27me3 microChIP as described in “ChIP-seq”. ChIP DNA was amplified by real-time quantitative PCR using SyberGreen (Applied

Author Manuscript Author Manuscript Author Manuscript Author Manuscript

Biosystems) on QuantStudio 6 Flex Real-Time PCR System (Applied Biosystems) and the primers in Table S5.

**RT-qPCR—**Between 50,000 and 100,000 naive B cells ($B220^+CD38^+Fas^-IgD^+$), centroblasts ($B220^+CD38^-Fas^+CXCR4^{hi}CD86^{lo}$) and centrocytes ($B220^+CD38^-Fas^+CXCR4^{lo}CD86^{hi}$) were sorted from spleens of 4 Cγ1-cre and 4 *Ezh2(Y641F)*$^{fl/WT}$;Cγ1-cre mice 8 days after SRBC immunization. RNA was prepared using Trizol extraction (Invitrogen). cDNA was prepared using cDNA synthesis kit (ThermoFisher Scientific) and detected by fast SyberGreen (Applied Biosystems) on QuantStudio 6 Flex Real-Time PCR System (Applied Biosystems) using the primers in Table S5. We normalized gene expression to *Hprt1*, *Rpl13* or *Gapdh*, according to the level of expression, and expressed values using the ΔCT method. Results were represented as fold expression with the standard deviation for 2 series of triplicates.

## Histone mass spectometry

**Histone extraction and preparation.:** Histones were extracted by direct sorting of GC and naive B cells into $H_2SO_4$ and cellular debris was removed by centrifugation at 4,000 x *g* for 5 minutes. Histones were precipitated from the supernatant by the addition of trichloroacetic acid (TCA) at a final concentration of 20% (v/v) overnight at 4 °C. Following centrifugation at 10,000 x *g* for 5 minutes, histone pellets were washed once with 0.1% HCl in acetone then 100% acetone with centrifugation at 15,000 x *g* for 5 minutes. Histones were dried briefly in a fume hood and stored at −80 °C until further processing. Derivatization and digestion was modified from (Garcia et al., 2007). Dried histones were resuspended in 50 mM ammonium bicarbonate (10 μL). Sodium hydroxide (5 μL) was added immediately followed by the addition of propionic anhydride (20 μL, 1:3 dilution in isopropanol). The pH was adjusted to 8 with additional sodium hydroxide then incubated at 52°C for 1 hour before drying to completion in a SpeedVac concentrator. Histones were digested for 16 hours with 1 μg trypsin, dried in a Speedvac concentrator and subjected to a final propionylation as described above.

**Targeted mass spectrometry.:** Histone peptides were resuspended in Loading Pump Solvent A (water with 0.1% TFA) and analyzed by nano-LC (Dionex) on a triple quadrupole mass spectrometer (TSQ Quantiva, ThermoFisher Scientific). Peptides were loaded on a trapping column (3 cm×150 μm, packed wi th ProntoSIL C18-AQ, 3μm, 200Å resin (New Objective) with 100% Loading Solvent A for 10 minutes at a flow rate of 2.5 μL/min then eluted from the trapping column and separated on a PicoChip analytical capillary column (10 cm × 75 μm packed with ProntoS IL C18-AQ, 3 μm, 200 Å resin (New Objective). The peptides were eluted from the analytical column using Nano Pump Solvent A (water with 0.1% formic acid) and Nano Pump Solvent B (95% acetonitrile with 0.1% formic acid) at 0.30 μL/min and increasing the percentage of Nano Pump Solvent B from 1 to 35% over 45 minutes. Ions were produced by electrospray from an emitter with a 10 μm tip (New Objective) and introduced into the mass spectrometer with the following settings: collision gas pressure of 1.5 mTorr; Q1 peak width of 0.7 (FWHM); cycle time of 3 seconds; skimmer offset of 10 V; electrospray voltage of 2.5 kV. All injections were performed in technical triplicate. Targeted analysis of unmodified and various modified histone peptides was

Author Manuscript Author Manuscript Author Manuscript Author Manuscript

performed with transitions specific to each peptide species as described previously (Zheng et al., 2012; Zheng et al., 2013).

**Quantitation of histone modifications.:** Raw mass spectometry files were analyzed with Skyline using Savitzky-Golay smoothing (MacLean et al., 2010) and peak area assignments were manually confirmed. Total peak areas exported from Skyline were used to calculate the relative abundances of each histone post-translational modifications. See Table S6 for relative abundance and peptide peak area quantification.

### Single cell immunoglobulin SHM assessment

**Isolation of cells and sequencing.:** Three R26-lox-stop-lox-YFP;Cγ1-cre, 3 R26-lox-stop-lox-YFP;Ezh2(Y641F)$^{fl/WT}$;Cγ1-cre, 3 R26R-Confetti;Cγ1-cre and 3 R26R-Confetti;Ezh2(Y641F)$^{fl/WT}$;Cγ1-cre fresh spleens from mice immunized with NP-OVA for 10 days were embedded in 2% low melt agarose and sectioned at 150 μm with a vibratome. Individual fluorescent GCs were identified by fluorescence microscopy, 5 to 10 GCs per spleen were extracted, single cell suspensions were prepared, cells were stained with GC B cell markers (B220, GL7, FAS, IgD) and single cell index sorted into TCL buffer (Qiagen) with 1% 2-mercaptoethanol. In the case of YFP GCs, cells were also stained with centroblast/centrocyte markers (CXCR4 and CD86) before sorting. RNA was extracted from single cells sorted into individual wells using SPRIselect beads (Beckman Coulter), converted to cDNA using anchored oligo dT(20), subjected to nested PCR for IgM and IgG1 variable regions, and used to bar-code, index and generate libraries for paired end 300 bp sequencing in MiSeq (Illumina), using primers and indexes as previously published (Ho et al., 2016; Tiller et al., 2009) (Figure S7A).

**Sequence processing.:** Raw reads were filtered to remove low quality sequences and build consensus sequences corresponding to barcoded wells. Preprocessing was performed using pRESTO v0.5.10 (Vander Heiden et al., 2014) as follows: 1) Reads less than 300bp in length were removed, as were reads with a mean Phred quality score below 20. 2) Forward reads without an exact match to a known index barcode from position 2–8bp and a valid forward primer starting at position 8bp with a maximum match error of 0.1 were removed. 3) To remove PCR chimera errors, forward reads which matched a forward primer anywhere in their sequence a second time were removed, with a maximum error rate of 0.1. 4) Reads which did not match a valid C region primer with a maximum error rate of 0.1 were also removed.

Initial analysis showed insufficient well index barcode diversity. To correct for this, 1) forward and reverse reads were concatenated and clustered using USearch v7.0.1090 (Edgar, 2010). 2) Separate consensus sequences from the forward and reverse reads within each of these barcode clusters were constructed with a maximum gap frequency of 0.5, and minimum consensus C region primer frequency of 0.6. 3) Using the pRESTO function AssemblePairs, forward and reverse consensus sequences were aligned to each other and assembled into sequences using a minimum overlapping length of 8, maximum error of 0.3, and a significance threshold (alpha) of $1x10^{-5}$.

Author Manuscript Author Manuscript Author Manuscript Author Manuscript

Following preprocessing, V(D)J assignment was performed using IgBLAST v1.13.0 (Ye et al., 2013) against the IMGT mouse germline reference database (IMGT/GENE-DB v3.1.22; retrieved April 3th, 2019) (Giudicelli et al., 2005). Only germline V-gene segments labeled as functional were included. Default IgBLAST parameters were used. Post processing of IgBLAST output and clonal clustering were performed using Change-O v0.4.5 (Gupta et al., 2015). The D segment and N/P regions of predicted un-mutated germline ancestors were masked by "N" nucleotides. Nonfunctional sequences and those with in-frame stop codons were removed.

Within each plate, sequences making up less than 50% of the read count for a particular well barcode were removed. Remaining sequences had a high frequency of identical sequence and barcode combinations among different mice (up to 14.5% of unique sequences; Figure S7G). These sequences tended to show high consensus count frequency in one plate, with a consensus count at least an order of magnitude lower in all other plates. To reduce this source of contamination, we removed all sequences in each sequencing run with a read count at or below a specified consensus count. Separate minimum consensus count cutoffs were chosen for the first (read count > 156) and second (read count > 174) YFP sequencing runs, as well as Confetti (read count > 62) such that each sequence and barcode combination occurred in at most one mouse. Across all 16 mice, 1186 total sequences were recovered.

**Clonal clustering.:** Within mice, sequences sharing a V and J gene annotation, junction length and differing from one another by a normalized Hamming distance of less than 0.1 within the junction region were clustered as clones via single-linkage hierarchical clustering using the DefineClones function in Change-O v0.4.5 (Gupta et al., 2017).

**Statistical analysis of sequence data.:** Statistical analyses were performed using custom scripts written in R v3.6.1 (R-Core-Team, 2017) using functions supplied in the packages Alakazam v0.3.0 (Gupta et al., 2015) and SHazaM v0.2.0 (Yaari et al., 2013). Gating for centroblasts and centrocytes was performed based on CXCR4 and CD86 fluorescence, with specific gating shown in Figure S7H.

Clonal diversity was characterized using the diversity index proposed by (Hill, 1973), and implemented in Alakazam v0.3.0 (Gupta et al., 2015). Similar to the analyses performed in (Vander Heiden et al., 2017), variability in sequencing depth was accounted for by rarefying each sample to 277 sequences for YFP mice and 178 sequences for Confetti mice, with 1000 realizations of repeated random sampling with replacement. A 95% confidence interval around each diversity estimate was calculated using the standard deviation of resampling realization (Chao et al., 2015). The significance of the difference in diversity score between groups was calculated using the delta of the resampling distribution between groups.

Sequences obtained from R26R-Confetti GCs were scored for fluorescence of GFP, CFP, RFP and YFP. To evaluate the ability of the 10 possible combinations of these colors to distinguish individual clones within each GC, sequences were grouped into clonal clusters based on their sequence similarity (see Clonal clustering above). The probability that two random sequences sampled with replacement were in the same clone was calculated using Simpson's diversity index (Simpson, 1949). The probability that two random sequences with

Author Manuscript Author Manuscript Author Manuscript Author Manuscript

the same color combination were in the same clone was calculated using an application of Bayes' rule (Eq. 1). This is equivalent to Simpson's diversity calculated on combined color/clone grouping (i.e., two random sequences having the same clone and color combination), divided by Simpson's diversity calculated for color groupings (i.e., two random sequences having the same color combination). These probabilities are shown in Table S7.

$$P(same\ clone \mid same\ color) = \frac{P(same\ clone\ and\ color)}{P(same\ color)} \quad (1)$$

To visualize how color combinations differed along clonal lineage development, lineage tree branch lengths and topologies were estimated by maximum parsimony using *dnapars* v3.697 (Felsenstein J., 2002, [PHYLIP] Phylogeny Inference Package, version 3.6a3). For lineage trees obtained from YFP mice, centroblast/centroctye state at each internal node was predicted using a straightforward maximum parsimony algorithm implemented within IgPhyML v1.1.1 (Hoehn et al., 2019). Clusters of zero-length branches were resolved to a maximum parsimony configuration using nearest neighbor interchange moves. Lineage trees and their associated color combinations (Figure S7F and Table S7) were visualized using the R package ggtree v1.16.0 (Yu et al., 2018; Yu et al., 2017).

To calculate internal/external branch length ratio, as well as trunk (branch leading immediately from the germline) and canopy (non-trunk branches) length ratio of YFP and Confetti mice (Figure 7D and 7J), we performed the following procedure for all trees with at least three non-identical sequences:

1. Sample the columns of each clonal lineage's multiple sequence alignment with replacement (i.e. take a single bootstrap replicate; (Felsenstein, 1985).
2. For each bootstrapped multiple sequence alignment, estimate lineage tree topologies and branch lengths using *dnapars* v3.697 (Felsenstein J., 2002, [PHYLIP] Phylogeny Inference Package, version 3.6a3).
3. For all WT trees, add all trunk branch lengths together and divide this number by the sum of all non-trunk branch lengths. This gives the trunk/canopy ratio of a single bootstrap replicate. Repeat this for $Ezh2^{Y641F}$ trees.
4. For all WT trees, add all internal (non-trunk) branch lengths together and divide this number by the sum of all non-trunk external branch lengths. This gives the internal/external branch length ratio of a single bootstrap replicate. Repeat this for $Ezh2^{Y641F}$ trees.

Repeat steps 1–4 1000 times, generating a bootstrapped distribution of these statistics.

## QUANTIFICATION AND STATISTICAL ANALYSIS

Statistical parameters including the exact value of n and precision measures (mean ± SEM or SD) and statistical significance are reported in the Figures and Figure Legends. Data is judged to be statistically significant when $p<0.05$ by two-tailed Student's t test. Asterisks in figures denote statistical significance as calculated by Student's t test (∗, $p<0.05$; ∗∗, $p<0.01$; ∗∗∗, $p<0.001$).

Author Manuscript Author Manuscript Author Manuscript Author Manuscript

Statistical analysis of Sequencing data is described under Method Details section and in Figure Legends.

**Quantification of CD45.1/CD45.2 cell ratios—**Tissue sections were stained for PNA, CD45.1 and CD45.2 and imaged at 40x in the confocal microscope. Since it is technically challenging to accurately delineate individual cells within the stained tissue sections, we decided to use the abundance of CD45.1 or CD45.2 positive pixels as a proxy for cell abundance within the GC. Following image acquisition, images were opened in ImageJ and GCs were manually delineated based on PNA staining and saved to create a GC mask. These GC masks were then overlaid as regions of interest (ROI) onto the CD45.1 and CD45.2 channels, to classify the GC region (set to 1), and the background—outside the m ask (set to 0). The GC region was then linearized (image region matrix to image vector), and intensity levels for CD45.1 and CD45.2 was recorded for each pixel within the ROI. Next, we plotted the intensity distributions for CD45.1 and CD45.2 and set appropriate thresholds to determine the number of positive pixels (real signal) based on pixel intensities, which was then visually confirmed. Of note, the thresholds were set to ensure that each pixel classified at CD45.1 positive was also consequently CD45.2 negative, and vice versa. Based on the thresholds per channel, we determined the number of positive pixels for CD45.1 and CD45.2, then calculated the positivity fraction of CD45.1 and CD45.2 within each GC.

**Quantification of FDC network size—**CD35 stained images of GC from the spleens of *Ezh2* WT or $Ezh2^{Y641F}$ mice were binarized, and a mask was created to define the FDC network region based on pixel positivity. Simultaneously, corresponding images of PNA stained GCs were traced and a binary mask of the region was delineated based on PNA positivity. Masks were then imported into Matlab where the binary images containing the masked regions were linearized and the size of the regions were computed as the number of pixels from each masked image having an index value of 1. Once the size of the regions was computed, the ratio of the CD35 mask (referred to as the FDC network size) and the PNA mask (GC size) was calculated. This was done for a series of images for at least 4 mice per condition, and the relative fraction was plotted.

**Quantification of proliferating cells within LZ and DZ—**Images from GCs containing the fluorescent FUCCI probe were acquired, and corresponding regions were stained with CD35 to outline the FDC regions. The FDC region was traced and binarized, and a mask was created for each FDC region per image. Simultaneously, the proliferating cells within the GCs, stained in green, were binarized and the binary images of both the proliferating cells and corresponding FDC mask was imported into Matlab. Once imported, the amount of proliferating cells within the FDC region (LZ) and outside the FDC region (DZ) was computed. The amount of proliferating cells within each region was calculated as the number of pixels having a value of 1 within each defined region. Using the number of pixels per region, the sum of pixels in each region was calculated, and the fraction of proliferation in the LZ was denoted as the amount of proliferation within the FDC region per total proliferation. Similarly, the DZ was computed as the amount of proliferation outside the FDC region per total proliferation.

Author Manuscript Author Manuscript Author Manuscript Author Manuscript

**Clonal diversity quantification of R26R-Confetti—**Multicolor confocal images were acquired using a Zeiss LSM 880 microscope for splenic GCs of immunized R26R-Confetti;Cγ1-cre and R26R-Confetti;*Ezh2(Y641F)*$^{fl/WT}$;Cγ1-cre mice. Following acquisition, 4-color compisite images were split into individual channels (YFP, GFP, RFP, and CFP), and binarized using Fiji/ImageJ. This binarization step converts the continuous intensity scale per image into a binary scale of '1' for the foreground and '0' for the background. This was done for all images within the image sequence per condition (each image is a GC), and the masks were saved for further analysis. Following this step, a subset of images were visually inspected and compared to the raw images to ensure that the binarization was acceptable. The four masks per image were loaded into Matlab, and the boundaries of each object was delineated. Next a composite image consisting of the object-boundaries (cells) were overlaid, and revealing the ten color combinations. Using the spatial overlap per object, the abundance of cells within each clone (each color combination) was enumerated. This image processing sequence performed well for most images, however in a subset of images we observed larger objects, likely corresponding to multiple cells. To circumvent this, we computed the average size (pixel area) of objects corresponding to individual cells, and the 'large object area' was divided by het average size of an individual cell per image. Once the abundance of each clone was computed, results were tabulated and plotted in a heat map per image. It was important not to combine the results from each image, since the abundance/dominance of each clone per GC is stochastic. To determine the degree of clonal diversity we computed the Shannon entropy per image.

$$S = \sum pi \,.\, \ln(pi)$$

where 'S' is the shannon entropy, and 'pi' is the bundance of cells within each state. To have a better understanding on what the magnitude of the Shannon entropy meant, we determined the Shannon entropies for two distributions illustrating extremes of clonal diversity for ten states each; uniform distribution—high clonal diversity (S=2.3) and Poisson distribution (k=1)—low clonal diversity (S= 0.94).

## DATA AND CODE AVAILABILITY

**Data resources—**Raw data files for the sequencing analysis have been deposited in the NCBI Gene Expression Omnibus under accession number GEO: GSE138037. This accession number is the master superseries for:

GSE138032: RNA-seq

GSE138033: single cell RNA-seq

GSE138036: ChIP-seq

**Code resources:** Sequence processing and analysis scripts of single cell immunoglobulin SHM are available at: https://bitbucket.org/kleinstein/melnick_gcb_scripts

Author Manuscript Author Manuscript Author Manuscript Author Manuscript

## Supplementary Material

Refer to Web version on PubMed Central for supplementary material.

## ACKNOWLEDGEMENTS

We thank Dr. Gabriel D. Victora and Dr. Luka Mesin (Rockefeller U) for their technical support to perform the single cell IgV sequencing from single GCs; Dr. Hao Shen, Juliet Philips and members of the Melnick lab; Dr. Jason Vander Heiden and Roy Jiang for advice in BCR sequence processing; Dr. Jason McCormick from WCM Flow Cytometry Core Facility; Dr. Sushmita Mukherjee from WCM Optical Microscopy Core, and Dr. Alicia Alonso from WCM Epigenomics Core. Histone mass spectrometry was performed at Northwestern Proteomics, supported by NCI CCSG P30 CA060553 awarded to the Robert H. Lurie Comprehensive Cancer Center and the National Resource for Translational and Developmental Proteomics, supported by P41 GM108569. A.M.M. and W.B. are supported by NCI R35 CA220499, LLS TRP 6572–19, LLS SCOR 7013–17. W.B. is also supported by ASH Junior Faculty Scholar Award. A.M.M. is also supported by NCI R01 CA198089, The Follicular Lymphoma Consortium and The Chemotherapy Foundation. S.H.K. is supported by NIH R01AI104739; A.A.S., by Damon Runyon Cancer Research Foundation; K.B.H., by PhRMA Foundation Post-doctoral Fellowship in Informatics; L.V., by LLS Career Development Program fellowship; K.T., by Uehara Memorial Foundation fellowship award. C.S. is supported by the Michael Smith Foundation for Health Research (Career Investigator Award) and received Program Project Grant funding from the Terry Fox Research Institute and the Canada LLS.

## REFERENCES

Anderson SM, Tomayko MM, Ahuja A, Haberman AM, and Shlomchik MJ (2007). New markers for murine memory B cells that define mutated and unmutated subsets. J Exp Med 204, 2103–2114. [PubMed: 17698588]

Beguelin W, Popovic R, Teater M, Jiang Y, Bunting KL, Rosen M, Shen H, Yang SN, Wang L, Ezponda T, et al. (2013). EZH2 is required for germinal center formation and somatic EZH2 mutations promote lymphoid transformation. Cancer Cell 23, 677–692. [PubMed: 23680150]

Beguelin W, Rivas MA, Calvo Fernandez MT, Teater M, Purwada A, Redmond D, Shen H, Challman MF, Elemento O, Singh A, and Melnick AM (2017). EZH2 enables germinal centre formation through epigenetic silencing of CDKN1A and an Rb-E2F1 feedback loop. Nat Commun 8, 877. [PubMed: 29026085]

Beguelin W, Teater M, Gearhart MD, Calvo Fernandez MT, Goldstein RL, Cardenas MG, Hatzi K, Rosen M, Shen H, Corcoran CM, et al. (2016). EZH2 and BCL6 Cooperate to Assemble CBX8-BCOR Complex to Repress Bivalent Promoters, Mediate Germinal Center Formation and Lymphomagenesis. Cancer Cell 30, 197–213. [PubMed: 27505670]

Benjamini Y, and Hochberg Y (1995). Controlling the False Discovery Rate: A Practical and Powerful Approach to Multiple Testing. Journal of the Royal Statistical Society.

Blanco E, Di Croce L, and Aranda S (2019). Comparative ChIP-seq (Comp-ChIP-seq): a novel computational methodology for genome-wide analysis. bioRxiv.

Bodor C, Grossmann V, Popov N, Okosun J, O'Riain C, Tan K, Marzec J, Araf S, Wang J, Lee AM, et al. (2013). EZH2 mutations are frequent and represent an early event in follicular lymphoma. Blood 122, 3165–3168. [PubMed: 24052547]

Brach D, Johnston-Blackwell D, Drew A, Lingaraj T, Motwani V, Warholic NM, Feldman I, Plescia C, Smith JJ, Copeland RA, et al. (2017). EZH2 Inhibition by Tazemetostat Results in Altered Dependency on B-cell Activation Signaling in DLBCL. Mol Cancer Ther 16, 2586–2597. [PubMed: 28835384]

Browning JL, Dougas I, Ngam-ek A, Bourdon PR, Ehrenfels BN, Miatkowski K, Zafari M, Yampaglia AM, Lawton P, Meier W, and et al. (1995). Characterization of surface lymphotoxin forms. Use of specific monoclonal antibodies and soluble receptors. J Immunol 154, 33–46. [PubMed: 7995952]

Caganova M, Carrisi C, Varano G, Mainoldi F, Zanardi F, Germain PL, George L, Alberghini F, Ferrarini L, Talukder AK, et al. (2013). Germinal center dysregulation by histone methyltransferase EZH2 promotes lymphomagenesis. J Clin Invest 123, 5009–5022. [PubMed: 24200695]

Author Manuscript Author Manuscript Author Manuscript Author Manuscript

Calado DP, Sasaki Y, Godinho SA, Pellerin A, Kochert K, Sleckman BP, de Alboran IM, Janz M, Rodig S, and Rajewsky K (2012). The cell-cycle regulator c-Myc is essential for the formation and maintenance of germinal centers. Nat Immunol 13, 1092–1100. [PubMed: 23001146]

Casola S, Cattoretti G, Uyttersprot N, Koralov SB, Seagal J, Hao Z, Waisman A, Egert A, Ghitza D, and Rajewsky K (2006). Tracking germinal center B cells expressing germ-line immunoglobulin gamma1 transcripts by conditional gene targeting. Proc Natl Acad Sci U S A 103, 7396–7401. [PubMed: 16651521]

Chao A, Hsieh TC, Chazdon RL, Colwell RK, and Gotelli NJ (2015). Unveiling the species-rank abundance distribution by generalizing the Good-Turing sample coverage theory. Ecology 96, 1189–1201. [PubMed: 26236834]

Chapuy B, Stewart C, Dunford AJ, Kim J, Kamburov A, Redd RA, Lawrence MS, Roemer MGM, Li AJ, Ziepert M, et al. (2018). Molecular subtypes of diffuse large B cell lymphoma are associated with distinct pathogenic mechanisms and outcomes. Nat Med 24, 679–690. [PubMed: 29713087]

Conway E, Healy E, and Bracken AP (2015). PRC2 mediated H3K27 methylations in cellular identity and cancer. Curr Opin Cell Biol 37, 42–48. [PubMed: 26497635]

Dobin A, Davis CA, Schlesinger F, Drenkow J, Zaleski C, Jha S, Batut P, Chaisson M, and Gingeras TR (2013). STAR: ultrafast universal RNA-seq aligner. Bioinformatics 29, 15–21. [PubMed: 23104886]

Dominguez-Sola D, Victora GD, Ying CY, Phan RT, Saito M, Nussenzweig MC, and Dalla-Favera R (2012). The proto-oncogene MYC is required for selection in the germinal center and cyclic reentry. Nat Immunol 13, 1083–1091. [PubMed: 23001145]

Donaldson-Collier MC, Sungalee S, Zufferey M, Tavernari D, Katanayeva N, Battistello E, Mina M, Douglass KM, Rey T, Raynaud F, et al. (2019). EZH2 oncogenic mutations drive epigenetic, transcriptional, and structural changes within chromatin domains. Nat Genet 51, 517–528. [PubMed: 30692681]

Edgar RC (2010). Search and clustering orders of magnitude faster than BLAST. Bioinformatics 26, 2460–2461. [PubMed: 20709691]

Elgueta R, Benson MJ, de Vries VC, Wasiuk A, Guo Y, and Noelle RJ (2009). Molecular mechanism and function of CD40/CD40L engagement in the immune system. Immunol Rev 229, 152–172. [PubMed: 19426221]

Ersching J, Efeyan A, Mesin L, Jacobsen JT, Pasqual G, Grabiner BC, Dominguez-Sola D, Sabatini DM, and Victora GD (2017). Germinal Center Selection and Affinity Maturation Require Dynamic Regulation of mTORC1 Kinase. Immunity 46, 1045–1058 e1046. [PubMed: 28636954]

Felsenstein J (1985). Confidence Limits on Phylogenies: An Approach Using the Bootstrap. Evolution 39, 783–791. [PubMed: 28561359]

Ferrari KJ, Scelfo A, Jammula S, Cuomo A, Barozzi I, Stutzer A, Fischle W, Bonaldi T, and Pasini D (2014). Polycomb-dependent H3K27me1 and H3K27me2 regulate active transcription and enhancer fidelity. Mol Cell 53, 49–62. [PubMed: 24289921]

Frankish A, Diekhans M, Ferreira AM, Johnson R, Jungreis I, Loveland J, Mudge JM, Sisu C, Wright J, Armstrong J, et al. (2019). GENCODE reference annotation for the human and mouse genomes. Nucleic Acids Res 47, D766–D773. [PubMed: 30357393]

Garcia BA, Mollah S, Ueberheide BM, Busby SA, Muratore TL, Shabanowitz J, and Hunt DF (2007). Chemical derivatization of histones for facilitated analysis by mass spectrometry. Nat Protoc 2, 933–938. [PubMed: 17446892]

Giudicelli V, Chaume D, and Lefranc MP (2005). IMGT/GENE-DB: a comprehensive database for human and mouse immunoglobulin and T cell receptor genes. Nucleic Acids Res 33, D256–261. [PubMed: 15608191]

Goodarzi H, Elemento O, and Tavazoie S (2009). Revealing global regulatory perturbations across human cancers. Mol Cell 36, 900–911. [PubMed: 20005852]

Green MR (2018). Chromatin modifying gene mutations in follicular lymphoma. Blood 131, 595–604. [PubMed: 29158360]

Green MR, Kihira S, Liu CL, Nair RV, Salari R, Gentles AJ, Irish J, Stehr H, Vicente-Duenas C, Romero-Camarero I, et al. (2015). Mutations in early follicular lymphoma progenitors are

Author Manuscript Author Manuscript Author Manuscript Author Manuscript

associated with suppressed antigen presentation. Proc Natl Acad Sci U S A 112, E1116–1125. [PubMed: 25713363]

Gulati N, Beguelin W, and Giulino-Roth L (2018). Enhancer of zeste homolog 2 (EZH2) inhibitors. Leuk Lymphoma 59, 1574–1585. [PubMed: 29473431]

Gupta NT, Adams KD, Briggs AW, Timberlake SC, Vigneault F, and Kleinstein SH (2017). Hierarchical Clustering Can Identify B Cell Clones with High Confidence in Ig Repertoire Sequencing Data. J Immunol 198, 2489–2499. [PubMed: 28179494]

Gupta NT, Vander Heiden JA, Uduman M, Gadala-Maria D, Yaari G, and Kleinstein SH (2015). Change-O: a toolkit for analyzing large-scale B cell immunoglobulin repertoire sequencing data. Bioinformatics 31, 3356–3358. [PubMed: 26069265]

Hansen KH, Bracken AP, Pasini D, Dietrich N, Gehani SS, Monrad A, Rappsilber J, Lerdrup M, and Helin K (2008). A model for transmission of the H3K27me3 epigenetic mark. Nat Cell Biol 10, 1291–1300. [PubMed: 18931660]

Hanzelmann S, Castelo R, and Guinney J (2013). GSVA: gene set variation analysis for microarray and RNA-seq data. BMC Bioinformatics 14, 7. [PubMed: 23323831]

Hill MO (1973). Diversity and evenness: a unifying notation and its consequences. Ecology 54, 427–432

Ho IY, Bunker JJ, Erickson SA, Neu KE, Huang M, Cortese M, Pulendran B, and Wilson PC (2016). Refined protocol for generating monoclonal antibodies from single human and murine B cells. J Immunol Methods 438, 67–70. [PubMed: 27600311]

Hoehn KB, Vander Heiden JA, Zhou JQ, Lunter G, Pybus OG, and Kleinstein S (2019). Repertoire-wide phylogenetic models of B cell molecular evolution reveal evolutionary signatures of aging and vaccination. bioRxiv, 558825.

Huang CY, Bredemeyer AL, Walker LM, Bassing CH, and Sleckman BP (2008). Dynamic regulation of c-Myc proto-oncogene expression during lymphocyte development revealed by a GFP-c-Myc knock-in mouse. Eur J Immunol 38, 342–349. [PubMed: 18196519]

Ise W, Fujii K, Shiroguchi K, Ito A, Kometani K, Takeda K, Kawakami E, Yamashita K, Suzuki K, Okada T, and Kurosaki T (2018). T Follicular Helper Cell-Germinal Center B Cell Interaction Strength Regulates Entry into Plasma Cell or Recycling Germinal Center Cell Fate. Immunity 48, 702–715 e704. [PubMed: 29669250]

Jackson CH (2008). Displaying Uncertainty With Shading. The American Statistician 62, 340–347.

Kline J, Godfrey J, and Ansell SM (2019). The Immune Landscape and Response to Immune Checkpoint Blockade Therapy in Lymphoma. Blood.

Knutson SK, Wigle TJ, Warholic NM, Sneeringer CJ, Allain CJ, Klaus CR, Sacks JD, Raimondi A, Majer CR, Song J, et al. (2012). A selective inhibitor of EZH2 blocks H3K27 methylation and kills mutant lymphoma cells. Nat Chem Biol 8, 890–896. [PubMed: 23023262]

Kridel R, Chan FC, Mottok A, Boyle M, Farinha P, Tan K, Meissner B, Bashashati A, McPherson A, Roth A, et al. (2016). Histological Transformation and Progression in Follicular Lymphoma: A Clonal Evolution Study. PLoS Med 13, e1002197. [PubMed: 27959929]

Laugesen A, Hojfeldt JW, and Helin K (2019). Molecular Mechanisms Directing PRC2 Recruitment and H3K27 Methylation. Mol Cell 74, 8–18. [PubMed: 30951652]

Lee E, Chuang HY, Kim JW, Ideker T, and Lee D (2008). Inferring pathway activity toward precise disease classification. PLoS Comput Biol 4, e1000217. [PubMed: 18989396]

Lee HG, Kahn TG, Simcox A, Schwartz YB, and Pirrotta V (2015). Genome-wide activities of Polycomb complexes control pervasive transcription. Genome Res 25, 1170–1181. [PubMed: 25986499]

Lefranc M-P, and Lefranc G (2001). The Immunoglobulin FactsBook).

Liao Y, Smyth GK, and Shi W (2014). featureCounts: an efficient general purpose program for assigning sequence reads to genomic features. Bioinformatics 30, 923–930. [PubMed: 24227677]

Liberzon A, Subramanian A, Pinchback R, Thorvaldsdottir H, Tamayo P, and Mesirov JP (2011). Molecular signatures database (MSigDB) 3.0. Bioinformatics 27, 1739–1740. [PubMed: 21546393]

Author Manuscript Author Manuscript Author Manuscript Author Manuscript

Liu D, Xu H, Shih C, Wan Z, Ma X, Ma W, Luo D, and Qi H (2015). T-B-cell entanglement and ICOSL-driven feed-forward regulation of germinal centre reaction. Nature 517, 214–218. [PubMed: 25317561]

Livet J, Weissman TA, Kang H, Draft RW, Lu J, Bennis RA, Sanes JR, and Lichtman JW (2007). Transgenic strategies for combinatorial expression of fluorescent proteins in the nervous system. Nature 450, 56–62. [PubMed: 17972876]

Lossos IS, and Gascoyne RD (2011). Transformation of follicular lymphoma. Best Pract Res Clin Haematol 24, 147–163. [PubMed: 21658615]

Love MI, Huber W, and Anders S (2014). Moderated estimation of fold change and dispersion for RNA-seq data with DESeq2. Genome Biol 15, 550. [PubMed: 25516281]

MacLean B, Tomazela DM, Shulman N, Chambers M, Finney GL, Frewen B, Kern R, Tabb DL, Liebler DC, and MacCoss MJ (2010). Skyline: an open source document editor for creating and analyzing targeted proteomics experiments. Bioinformatics 26, 966–968. [PubMed: 20147306]

Margueron R, Justin N, Ohno K, Sharpe ML, Son J, Drury WJ 3rd, Voigt P, Martin SR, Taylor WR, De Marco V, et al. (2009). Role of the polycomb protein EED in the propagation of repressive histone marks. Nature 461, 762–767. [PubMed: 19767730]

Mayer CT, Gazumyan A, Kara EE, Gitlin AD, Golijanin J, Viant C, Pai J, Oliveira TY, Wang Q, Escolano A, et al. (2017). The microanatomic segregation of selection by apoptosis in the germinal center. Science 358.

McCabe MT, Graves AP, Ganji G, Diaz E, Halsey WS, Jiang Y, Smitheman KN, Ott HM, Pappalardi MB, Allen KE, et al. (2012a). Mutation of A677 in histone methyltransferase EZH2 in human B-cell lymphoma promotes hypertrimethylation of histone H3 on lysine 27 (H3K27). Proc Natl Acad Sci U S A 109, 2989–2994. [PubMed: 22323599]

McCabe MT, Ott HM, Ganji G, Korenchuk S, Thompson C, Van Aller GS, Liu Y, Graves AP, Della Pietra A 3rd, Diaz E, et al. (2012b). EZH2 inhibition as a therapeutic strategy for lymphoma with EZH2-activating mutations. Nature 492, 108–112. [PubMed: 23051747]

Mesin L, Ersching J, and Victora GD (2016). Germinal Center B Cell Dynamics. Immunity 45, 471–482. [PubMed: 27653600]

Meyer-Hermann ME, Maini PK, and Iber D (2006). An analysis of B cell selection mechanisms in germinal centers. Math Med Biol 23, 255–277. [PubMed: 16707510]

Mlynarczyk C, Fontan L, and Melnick A (2019). Germinal center-derived lymphomas: The darkest side of humoral immunity. Immunol Rev 288, 214–239. [PubMed: 30874354]

Morin RD, Johnson NA, Severson TM, Mungall AJ, An J, Goya R, Paul JE, Boyle M, Woolcock BW, Kuchenbauer F, et al. (2010). Somatic mutations altering EZH2 (Tyr641) in follicular and diffuse large B-cell lymphomas of germinal-center origin. Nat Genet 42, 181–185. [PubMed: 20081860]

Mort RL, Ford MJ, Sakaue-Sawano A, Lindstrom NO, Casadio A, Douglas AT, Keighren MA, Hohenstein P, Miyawaki A, and Jackson IJ (2014). Fucci2a: a bicistronic cell cycle reporter that allows Cre mediated tissue specific expression in mice. Cell Cycle 13, 2681–2696. [PubMed: 25486356]

Ngo VN, Korner H, Gunn MD, Schmidt KN, Riminton DS, Cooper MD, Browning JL, Sedgwick JD, and Cyster JG (1999). Lymphotoxin alpha/beta and tumor necrosis factor are required for stromal cell expression of homing chemokines in B and T cell areas of the spleen. J Exp Med 189, 403–412. [PubMed: 9892622]

Okosun J, Bodor C, Wang J, Araf S, Yang CY, Pan C, Boller S, Cittaro D, Bozek M, Iqbal S, et al. (2014). Integrated genomic analysis identifies recurrent mutations and evolution patterns driving the initiation and progression of follicular lymphoma. Nat Genet 46, 176–181. [PubMed: 24362818]

Oksuz O, Narendra V, Lee CH, Descostes N, LeRoy G, Raviram R, Blumenberg L, Karch K, Rocha PP, Garcia BA, et al. (2018). Capturing the Onset of PRC2-Mediated Repressive Domain Formation. Mol Cell 70, 1149–1162 e1145. [PubMed: 29932905]

Oprea M, and Perelson AS (1997). Somatic mutation leads to efficient affinity maturation when centrocytes recycle back to centroblasts. J Immunol 158, 5155–5162. [PubMed: 9164931]

Author Manuscript Author Manuscript Author Manuscript Author Manuscript

Orlando DA, Chen MW, Brown VE, Solanki S, Choi YJ, Olson ER, Fritz CC, Bradner JE, and Guenther MG (2014). Quantitative ChIP-Seq normalization reveals global modulation of the epigenome. Cell Rep 9, 1163–1170. [PubMed: 25437568]

Ortega-Molina A, Boss IW, Canela A, Pan H, Jiang Y, Zhao C, Jiang M, Hu D, Agirre X, Niesvizky I, et al. (2015). The histone lysine methyltransferase KMT2D sustains a gene expression program that represses B cell lymphoma development. Nat Med 21, 1199–1208. [PubMed: 26366710]

Ott HM, Graves AP, Pappalardi MB, Huddleston M, Halsey WS, Hughes AM, Groy A, Dul E, Jiang Y, Bai Y, et al. (2014). A687V EZH2 is a driver of histone H3 lysine 27 (H3K27) hypertrimethylation. Mol Cancer Ther 13, 3062–3073. [PubMed: 25253781]

Papa I, and Vinuesa CG (2018). Synaptic Interactions in Germinal Centers. Front Immunol 9, 1858. [PubMed: 30150988]

R-Core-Team (2017). R: A Language and Environment for Statistical Computing. R Foundation for Statistical Computing, Vienna, Austria.

Rajewsky K, Forster I, and Cumano A (1987). Evolutionary and somatic selection of the antibody repertoire in the mouse. Science 238, 1088–1094. [PubMed: 3317826]

Ramirez F, Dundar F, Diehl S, Gruning BA, and Manke T (2014). deepTools: a flexible platform for exploring deep-sequencing data. Nucleic Acids Res 42, W187–191. [PubMed: 24799436]

Reddy A, Zhang J, Davis NS, Moffitt AB, Love CL, Waldrop A, Leppa S, Pasanen A, Meriranta L, Karjalainen-Lindsberg ML, et al. (2017). Genetic and Functional Drivers of Diffuse Large B Cell Lymphoma. Cell 171, 481–494 e415. [PubMed: 28985567]

Robinson MD, and Oshlack A (2010). A scaling normalization method for differential expression analysis of RNA-seq data. Genome Biol 11, R25. [PubMed: 20196867]

Saelens W, Cannoodt R, Todorov H, and Saeys Y (2019). A comparison of single-cell trajectory inference methods. Nat Biotechnol 37, 547–554. [PubMed: 30936559]

Schindelin J, Arganda-Carreras I, Frise E, Kaynig V, Longair M, Pietzsch T, Preibisch S, Rueden C, Saalfeld S, Schmid B, et al. (2012). Fiji: an open-source platform for biological-image analysis. Nat Methods 9, 676–682. [PubMed: 22743772]

Schmitz R, Wright GW, Huang DW, Johnson CA, Phelan JD, Wang JQ, Roulland S, Kasbekar M, Young RM, Shaffer AL, et al. (2018). Genetics and Pathogenesis of Diffuse Large B-Cell Lymphoma. N Engl J Med 378, 1396–1407. [PubMed: 29641966]

Schwammle V, and Jensen ON (2010). A simple and fast method to determine the parameters for fuzzy c-means cluster analysis. Bioinformatics 26, 2841–2848. [PubMed: 20880957]

Scott DW, and Gascoyne RD (2014). The tumour microenvironment in B cell lymphomas. Nat Rev Cancer 14, 517–534. [PubMed: 25008267]

Shlomchik MJ, Luo W, and Weisel F (2019). Linking signaling and selection in the germinal center. Immunol Rev 288, 49–63. [PubMed: 30874353]

Simpson EH (1949). Measurement of Diversity. Nature 163, 688.

Sneeringer CJ, Scott MP, Kuntz KW, Knutson SK, Pollock RM, Richon VM, and Copeland RA (2010). Coordinated activities of wild-type plus mutant EZH2 drive tumor-associated hypertrimethylation of lysine 27 on histone H3 (H3K27) in human B-cell lymphomas. Proc Natl Acad Sci U S A 107, 20980–20985. [PubMed: 21078963]

Souroullas GP, Jeck WR, Parker JS, Simon JM, Liu JY, Paulk J, Xiong J, Clark KS, Fedoriw Y, Qi J, et al. (2016). An oncogenic Ezh2 mutation induces tumors through global redistribution of histone 3 lysine 27 trimethylation. Nat Med 22, 632–640. [PubMed: 27135738]

Stewart I, Radtke D, Phillips B, McGowan SJ, and Bannard O (2018). Germinal Center B Cells Replace Their Antigen Receptors in Dark Zones and Fail Light Zone Entry when Immunoglobulin Gene Mutations are Damaging. Immunity 49, 477–489 e477. [PubMed: 30231983]

Street K, Risso D, Fletcher RB, Das D, Ngai J, Yosef N, Purdom E, and Dudoit S (2018). Slingshot: cell lineage and pseudotime inference for single-cell transcriptomics. BMC Genomics 19, 477. [PubMed: 29914354]

Stuart T, Butler A, Hoffman P, Hafemeister C, Papalexi E, Mauck WM 3rd, Hao Y, Stoeckius M, Smibert P, and Satija R (2019). Comprehensive Integration of Single-Cell Data. Cell 177, 1888–1902 e1821. [PubMed: 31178118]

Author Manuscript Author Manuscript Author Manuscript Author Manuscript

Subramanian A, Tamayo P, Mootha VK, Mukherjee S, Ebert BL, Gillette MA, Paulovich A, Pomeroy SL, Golub TR, Lander ES, and Mesirov JP (2005). Gene set enrichment analysis: a knowledge-based approach for interpreting genome-wide expression profiles. Proc Natl Acad Sci U S A 102, 15545–15550. [PubMed: 16199517]

Tiller T, Busse CE, and Wardemann H (2009). Cloning and expression of murine Ig genes from single B cells. J Immunol Methods 350, 183–193. [PubMed: 19716372]

Vander Heiden JA, Stathopoulos P, Zhou JQ, Chen L, Gilbert TJ, Bolen CR, Barohn RJ, Dimachkie MM, Ciafaloni E, Broering TJ, et al. (2017). Dysregulation of B Cell Repertoire Formation in Myasthenia Gravis Patients Revealed through Deep Sequencing. J Immunol 198, 1460–1473. [PubMed: 28087666]

Vander Heiden JA, Yaari G, Uduman M, Stern JN, O'Connor KC, Hafler DA, Vigneault F, and Kleinstein SH (2014). pRESTO: a toolkit for processing high-throughput sequencing raw reads of lymphocyte receptor repertoires. Bioinformatics 30, 1930–1932. [PubMed: 24618469]

Velichutina I, Shaknovich R, Geng H, Johnson NA, Gascoyne RD, Melnick AM, and Elemento O (2010). EZH2-mediated epigenetic silencing in germinal center B cells contributes to proliferation and lymphomagenesis. Blood 116, 5247–5255. [PubMed: 20736451]

Victora GD, and Nussenzweig MC (2012). Germinal centers. Annu Rev Immunol 30, 429–457. [PubMed: 22224772]

Victora GD, Schwickert TA, Fooksman DR, Kamphorst AO, Meyer-Hermann M, Dustin ML, and Nussenzweig MC (2010). Germinal center dynamics revealed by multiphoton microscopy with a photoactivatable fluorescent reporter. Cell 143, 592–605. [PubMed: 21074050]

Xu S, Grullon S, Ge K, and Peng W (2014). Spatial clustering for identification of ChIP-enriched regions (SICER) to map regions of histone methylation patterns in embryonic stem cells. Methods Mol Biol 1150, 97–111. [PubMed: 24743992]

Yaari G, Vander Heiden JA, Uduman M, Gadala-Maria D, Gupta N, Stern JN, O'Connor KC, Hafler DA, Laserson U, Vigneault F, and Kleinstein SH (2013). Models of somatic hypermutation targeting and substitution based on synonymous mutations from high-throughput immunoglobulin sequencing data. Front Immunol 4, 358. [PubMed: 24298272]

Yap DB, Chu J, Berg T, Schapira M, Cheng SW, Moradian A, Morin RD, Mungall AJ, Meissner B, Boyle M, et al. (2011). Somatic mutations at EZH2 Y641 act dominantly through a mechanism of selectively altered PRC2 catalytic activity, to increase H3K27 trimethylation. Blood 117, 2451–2459. [PubMed: 21190999]

Ye J, Ma N, Madden TL, and Ostell JM (2013). IgBLAST: an immunoglobulin variable domain sequence analysis tool. Nucleic Acids Res 41, W34–40. [PubMed: 23671333]

Yu D, Cook MC, Shin DM, Silva DG, Marshall J, Toellner KM, Havran WL, Caroni P, Cooke MP, Morse HC, et al. (2008). Axon growth and guidance genes identify T-dependent germinal centre B cells. Immunol Cell Biol 86, 3–14. [PubMed: 17938642]

Yu G, Lam TT, Zhu H, and Guan Y (2018). Two Methods for Mapping and Visualizing Associated Data on Phylogeny Using Ggtree. Mol Biol Evol 35, 3041–3043. [PubMed: 30351396]

Yu G, Smith DK, Zhu H, Guan Y, and Lam TT-Y (2017). ggtree: an r package for visualization and annotation of phylogenetic trees with their covariates and other associated data. Methods in Ecology and Evolution 8, 28–36.

Zaretsky I, Atrakchi O, Mazor RD, Stoler-Barak L, Biram A, Feigelson SW, Gitlin AD, Engelhardt B, and Shulman Z (2017). ICAMs support B cell interactions with T follicular helper cells and promote clonal selection. J Exp Med 214, 3435–3448. [PubMed: 28939548]

Zheng Y, Sweet SM, Popovic R, Martinez-Garcia E, Tipton JD, Thomas PM, Licht JD, and Kelleher NL (2012). Total kinetic analysis reveals how combinatorial methylation patterns are established on lysines 27 and 36 of histone H3. Proc Natl Acad Sci U S A 109, 13549–13554. [PubMed: 22869745]

Zheng Y, Thomas PM, and Kelleher NL (2013). Measurement of acetylation turnover at distinct lysines in human histones identifies long-lived acetylation sites. Nat Commun 4, 2203. [PubMed: 23892279]

Author Manuscript Author Manuscript Author Manuscript Author Manuscript

## SIGNIFICANCE

We show that FL-associated *EZH2* mutation reprograms immune synapse functions to relieve GC B cells from requiring T cell help and to induce dependency on FDCs. *EZH2* mutations thus initiate lymphomagenesis through reprogramming of the immunological niche. This biological gain-of-function goes beyond the role of WT EZH2 in repressing GC differentiation and cell cycle checkpoint gene expression. These data may explain why EZH2 inhibitors are highly active and yet take a long time to manifest their full effect in *EZH2* mutant FLs, as remodeling of immune microenvironments might be a slow process. The data may also explain the relative inactivity of T cell therapies in FL and point to targeted therapy of FDCs as a potential alternative approach.

Author Manuscript Author Manuscript Author Manuscript Author Manuscript

## HIGHLIGHTS

- *EZH2* mutations initiate lymphomagenesis by reprogramming the GC microenvironment
- *EZH2* mutation attenuates B cell requirement for T cell help
- Mutant EZH2 drives expansion of GC centrocytes that are dependent on FDCs
- Mutant EZH2 establishes the characteristic follicular lymphoma immunological niche

Author Manuscript Author Manuscript Author Manuscript Author Manuscript

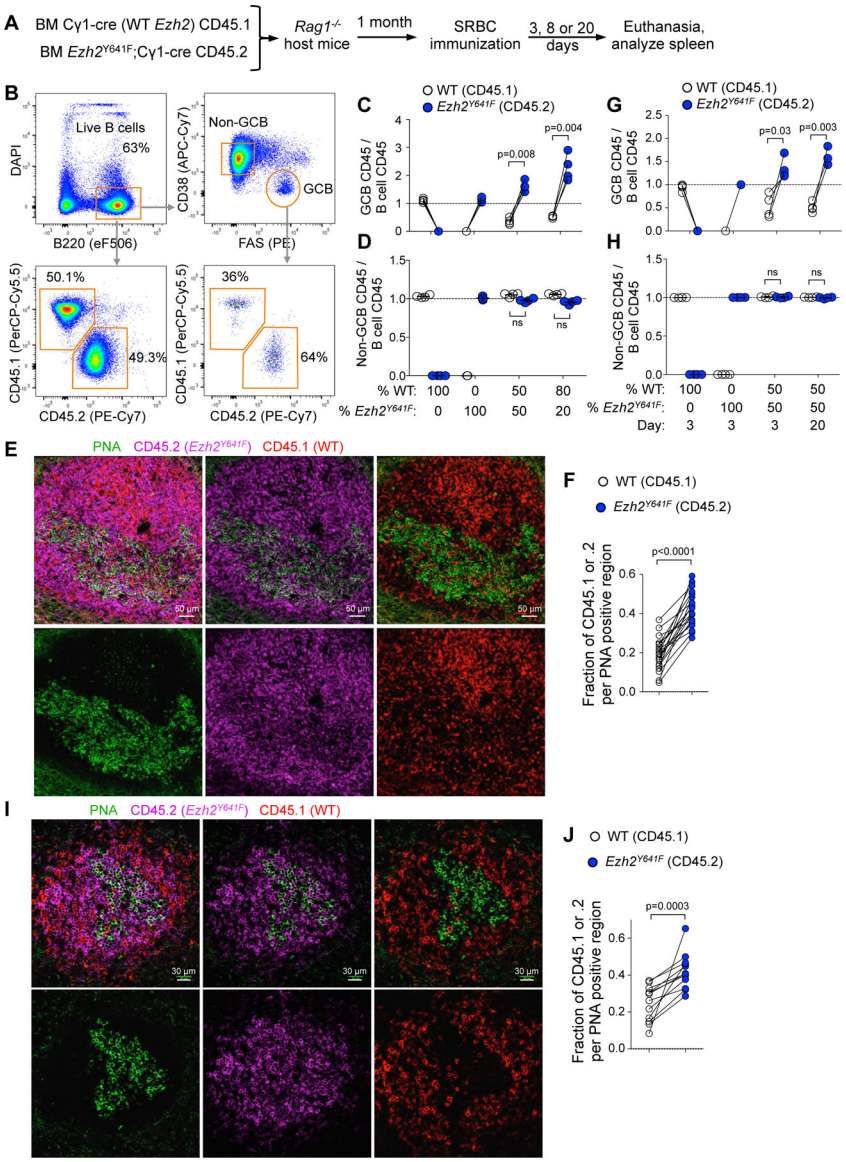


**Figure 1. Mutant *Ezh2* provides an advantage to activated B cells in expanding the GC reaction**

**A**. WT bone marrow (BM) (CD45.1) mixed with *Ezh2*$^{Y641F}$ BM (CD45.2) was injected into *Rag1*$^{-/-}$ mice, SRBC-immunized and euthanized 3, 8 or 20 days later.

**B**. Gating strategy of splenocytes of one representative sample.

**C**. Flow cytometry data of mice immunized for 8 days was analyzed by normalizing the percentage of CD45.1$^{+}$ GC B cells (CD38$^{-}$FAS$^{+}$) to their parental CD45.1$^{+}$ B cells (B220$^{+}$DAPI$^{-}$), and equivalent normalization with CD45.2$^{+}$ populations. Each pair of connected dots represents a mouse (n=4); paired t tests.

**D**. Analysis of non-GC B cells (CD38$^{+}$FAS$^{-}$) at day 8 was done as in **C**.

**E**. IF confocal microscopy images of chimeric splenic GCs at day 8 post-SRBC.

**F**. Quantification of PNA fluorescence was overlapped with CD45.1 and CD45.2 shown in **E** (and non-shown images), each pair of connected dots representing a single GC; paired t tests.

Author Manuscript Author Manuscript Author Manuscript Author Manuscript

**G-H**. Analysis of GC B cells (**G**) and non-GC B cells (**H**) at days 3 and 20 post-SRBC were done as in **C** (n=4 per group).

**I**. IF confocal microscopy images of chimeric splenic GCs at day 3 post-SRBC.

**J**. Quantification of GCs shown in **I** (and non-shown images) was done as in **F**.

Results at day 8 are representative of 3 independent experiments.

See also Figure S1.

Author Manuscript Author Manuscript Author Manuscript Author Manuscript

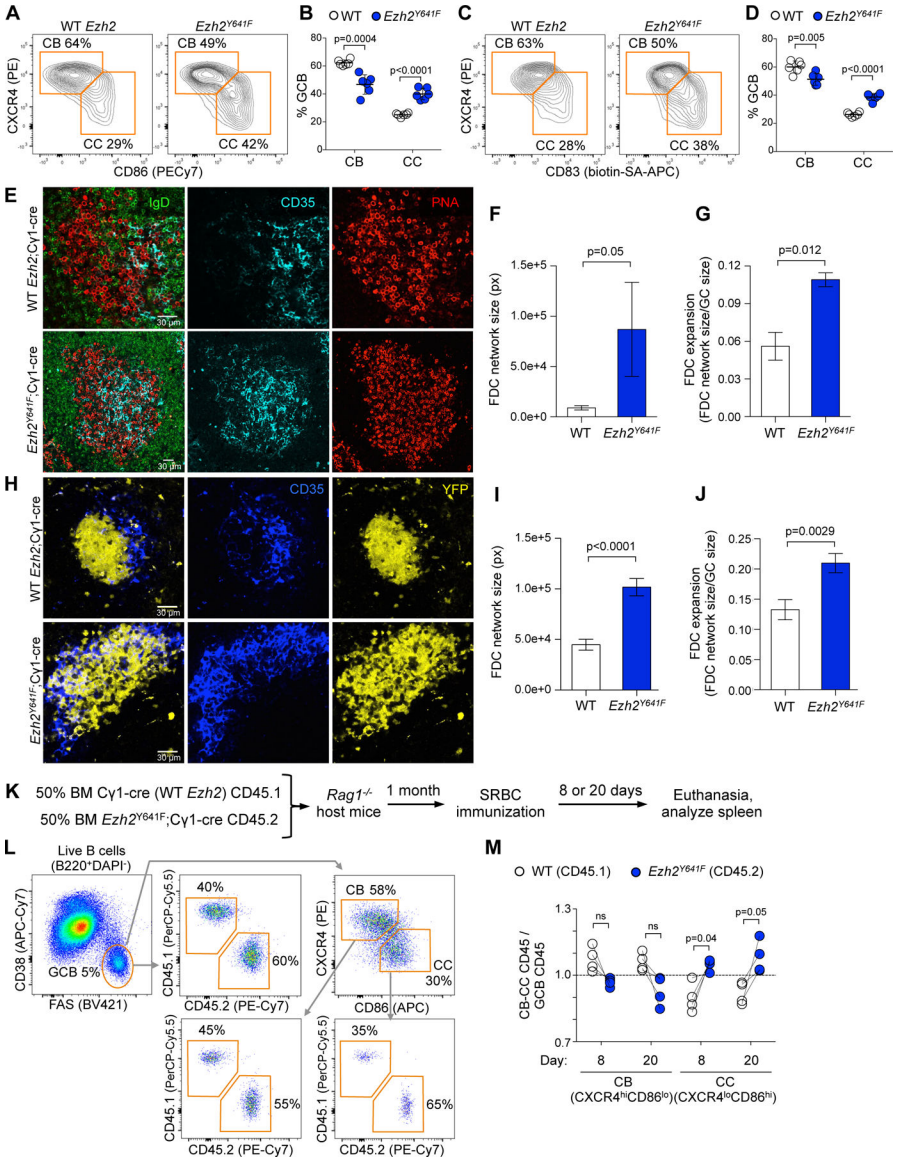


**Figure 2. Mutant *Ezh2* induces LZ expansion**

**A**. *Ezh2*$^{Y641F}$ and WT mice were SRBC-immunized for 8 days and spleens analyzed by flow cytometry. Centroblasts (CB) and centrocytes (CC) were gated from GC B cells.

**B**. Percentage of CBs and CCs shown in **A**. Each dot represents a mouse (n=6), mean ± SEM; unpaired t tests.

**C**. Flow cytometry data of splenocytes shown in **A**, using a different CC marker.

**D**. Percentage of CBs and CCs shown in **C**. Data shown as in **B**.

**E**. IF confocal microscopy images of splenic GCs at day 8 post-SRBC.

**F-G**. Quantification of FDC network size (**F**) and expansion (**G**) from IF images from 3 WT and 3 *Ezh2*$^{Y641F}$; mean ± SEM; unpaired t tests.

**H**. IF confocal microscopy images of YFP splenic GCs at day 8 post-SRBC. Mice were injected with anti CD35-BV421 to mark FDCs.

Author Manuscript Author Manuscript Author Manuscript Author Manuscript

**I-J**. Quantification of FDC network size (**I**) and expansion (**J**) from IF images from 5 YFP;*Ezh2*$^{Y641F}$ and 5 YFP;Cγ1-cre mice; mean ± SEM; unpaired t tests.

**K**. WT BM (CD45.1) mixed with *Ezh2*$^{Y641F}$ BM (CD45.2) was injected into *Rag1*$^{-/-}$ mice, SRBC-immunized and euthanized 8 or 20 days later.

**L**. Gating strategy of splenocytes of one representative sample.

**M**. Flow cytometry data was analyzed by normalizing the percentage of CD45.1$^{+}$ CBs (CXCR4$^{hi}$CD86$^{lo}$) and CCs (CXCR4$^{lo}$CD86$^{hi}$) to their parental CD45.1$^{+}$ GC B cells (CD38$^{-}$FAS$^{+}$), and equivalent normalization with CD45.2$^{+}$ populations. Each pair of connected dots represents a mouse (n=4); paired t tests.

Results representative of 3 to 4 experiments.

See also Figure S2.

Author Manuscript Author Manuscript Author Manuscript Author Manuscript

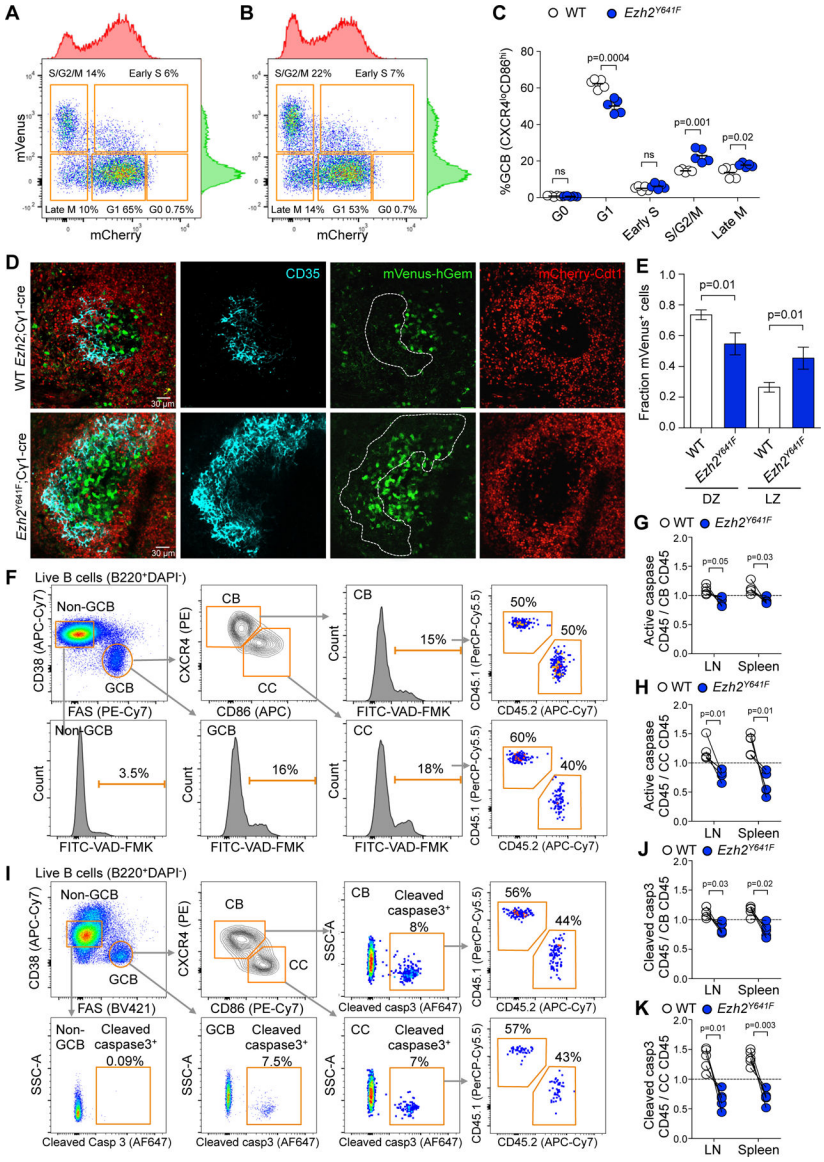


**Figure 3. *Ezh2* mutation causes aberrant proliferation and less apoptosis in the LZ**

**A-B**. Flow cytometry plots of splenic CCs (CXCR4$^{lo}$CD86$^{hi}$) of R26-Fucci2aR;Cγ1-cre (**A**) and R26-Fucci2aR;*Ezh2*$^{Y641F}$ (**B**) mice immunized with SRBC for 8 days.

**C**. Percentage of CCs shown in **A** and **B** at different cell cycle phases. Each dot represents a mouse (n=5), mean ± SEM; unpaired t tests.

**D**. IF confocal microscopy images of R26-Fucci2aR splenic GCs at day 8 post-SRBC. Mice were injected with anti CD35-BV421 to mark FDCs.

**E**. Quantification of proliferating mVenus$^{+}$ cells in images taken from 4 R26-Fucci2aR;Cγ1-cre and 4 R26-Fucci2aR;*Ezh2*$^{Y641F}$ mice; mean ± SEM; unpaired t tests.

**F**. Gating strategy of lymph node cells of mixed chimera mice generated as in Figure 2K and immunized with NP-OVA for 8 days. Apoptosis was assessed using VAD-FMK pan-caspase inhibitor.

Author Manuscript Author Manuscript Author Manuscript Author Manuscript

**G-H**. The percentage of CD45.1$^+$ VAD-FMK$^+$ splenocytes and lymph node (LN) cells was normalized to their parental CD45.1$^+$ CBs (**G**) and CCs (**H**), and equivalent normalization with CD45.2$^+$ populations, gated as shown in **F**. Each pair of connected dots represents a mouse (n=4); paired t tests.

**I**. Gating strategy of splenocytes of mixed chimera mice immunized with NP-OVA for 8 days. Apoptosis was assessed using an anti-cleaved caspase 3 antibody.

**J-K**. The percentages of CD45$^+$ cleaved caspase 3$^+$ cells shown in **I** were normalized to parental CBs (**J**) and CCs (**K**), and quantified as in **G-H**; n=4, paired t tests.

Results representative of 3 experiments.

See also Figure S3.

Author Manuscript Author Manuscript Author Manuscript Author Manuscript

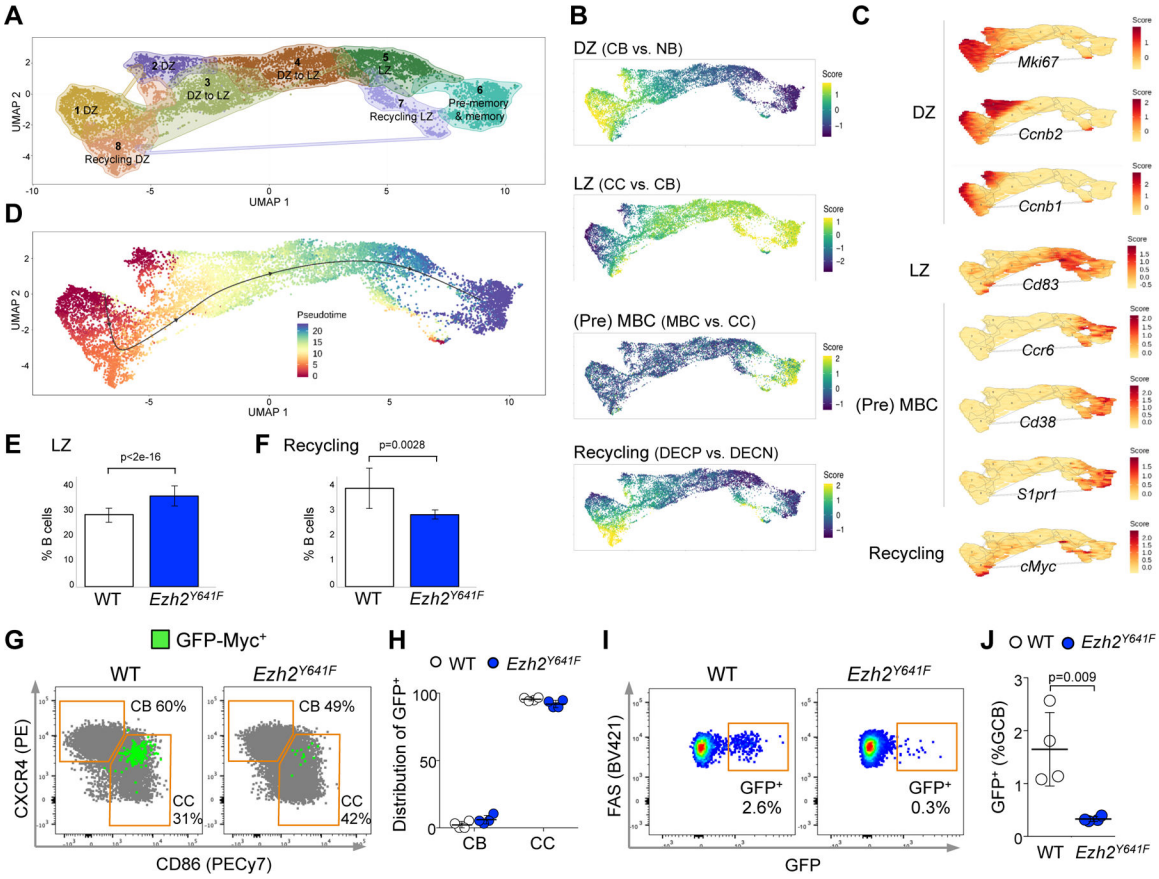


**Figure 4. Mutant *Ezh2* centrocytes fail to re-enter the DZ**

**A**. YFP$^{+}$IgD$^{-}$ splenocytes sorted from 3 YFP;*Ezh2*$^{Y641F}$ and 3 YFP;Cγ1-cre mice immunized with SRBC for 8 days were subjected to single cell RNA-seq. Dimensionality reduction with UMAP was performed on normalized gene expression values, using graph based clustering and K nearest neighbor analysis to assign cells to clusters with distinct expression profiles.

**B**. Mature B cell signatures were projected on clusters defined in **A**. MBC: memory B cell. DECP are positively selected GC B cells (Ersching et al., 2017).

**C**. Specific gene expressions were projected on clusters from **A**. **D**. Gene expression profiles were organized into a pseudotime vector by Slingshot.

**E-F**. After normalization for total number of analyzed cells, the abundance of *Ezh2*$^{Y641F}$ and WT was calculated for CC (LZ) (**E**) and recycling cells (**F**), based on the projected signature score from (**B**); data are mean ± SE (n=3 mice), p values generalized linear model.

**G**. GFP-Myc mice were SRBC-immunized for 8 days and spleens analyzed by flow cytometry. CBs and CCs were gated from GC B cells.

**H**. Total GFP$^{+}$ GC B cells were assigned to CBs and CCs, gated as shown in **G**. Each dot represents a mouse (n=4), mean ± SEM.

**I**. Flow cytometry plots showing the percentage of GFP$^{+}$ cells among GC B splenocytes from GFP-Myc mice.

**J**. Quantification of GFP$^{+}$ cells among GC B splenocytes from 4 GFP-Myc;*Ezh2*$^{Y641F}$ and 4 GFP-Myc;Cγ1-cre mice; mean ± SEM; unpaired t test.

Author Manuscript Author Manuscript Author Manuscript Author Manuscript

Results representative of 2 experiments.
See also Figure S4.

Author Manuscript Author Manuscript Author Manuscript Author Manuscript

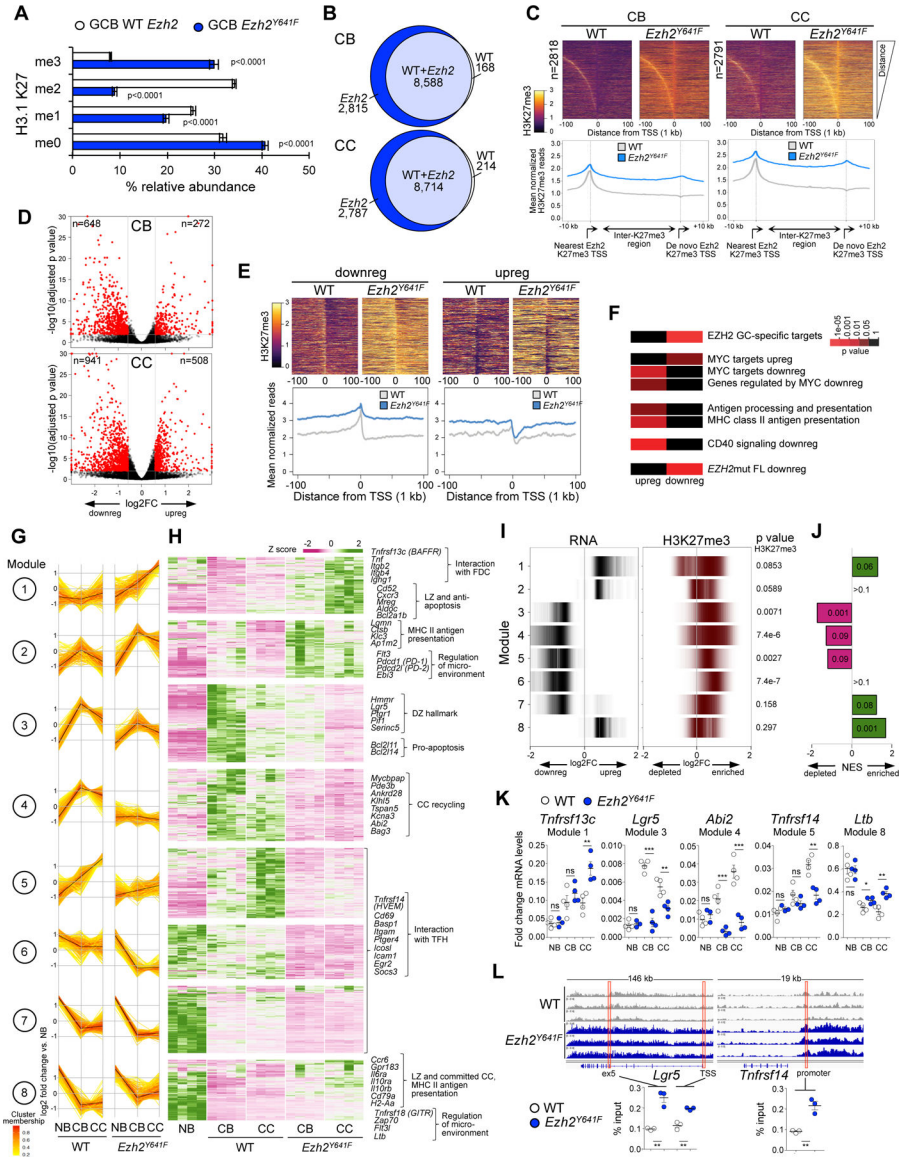

**Figure 5. *Ezh2* mutation produces transcriptional repression and spreading of H3K27me3 surrounding TSS sites**

**A**. Relative abundance of H3.1K27 by liquid chromatography separation and mass spectrometry of histones from SRBC-immunized mice (n=5). Mean ± SEM; unpaired t test.

**B**. H3K27me3 bound promoters by ChIP-seq (n=3 mice).

**C**. H3K27me3 normalized read density heat maps at $Ezh2^{Y641F}$-specific H3K27me3 promoters (top), and scaled H3K27me3 mean density plots of region between $Ezh2^{Y641F}$-specific H3K27me3 TSS and nearest TSS (bottom).

**D**. RNA-seq (n=4 mice); transcripts in red, fold-change>1.5, q<0.01.

**E**. H3K27me3 normalized read density heat maps at promoters of differentially expressed genes in CC (top), and mean H3K27me3 profile across loci interval (bottom).

**F**. Pathway analysis in CC.

**G-H**. Fuzzy c-means clustering of RNA-seq data: line plot (**G**) and heatmap (**H**) of standardized log2 fold-change relative to normal naive B (NB) cells. Black lines in (**G**) are

Author Manuscript Author Manuscript Author Manuscript Author Manuscript

cluster centroid; each gene is colored by the degree of cluster membership. Heatmap in (**H**) are z-scores of log2 fold-change values for each gene relative to NB.

**I**. RNA-seq and H3K27me3 profiles of *Ezh2*$^{Y641F}$ vs. WT CC per module. H3K27me3 enrichment, Wilcoxon test.

**J**. GSEA of murine CC *Ezh2*$^{Y641F}$ gene modules against gene expression of *EZH2* mutant FL cases vs. human CC.

**K**. RT-qPCR in NB, CB and CC (n=4). Each dot represents a mouse, mean fold change mRNA levels normalized to *Hprt1* (*Abi2*), *Gapdh* (*Lgr5*) or *Rpl13* (*Tnfrsf13c*,*Tnfrsf14* and *Ltb*) ± SEM; unpaired t test, **p<0.01, ***p<0.001.

**L**. H3K27me3 ChIP-seq tracks and qChIP validation in CC. Each dot represents a mouse (n=3), mean ± SEM; unpaired t test, **p<0.01.

See also Figure S5.

Author Manuscript Author Manuscript Author Manuscript Author Manuscript

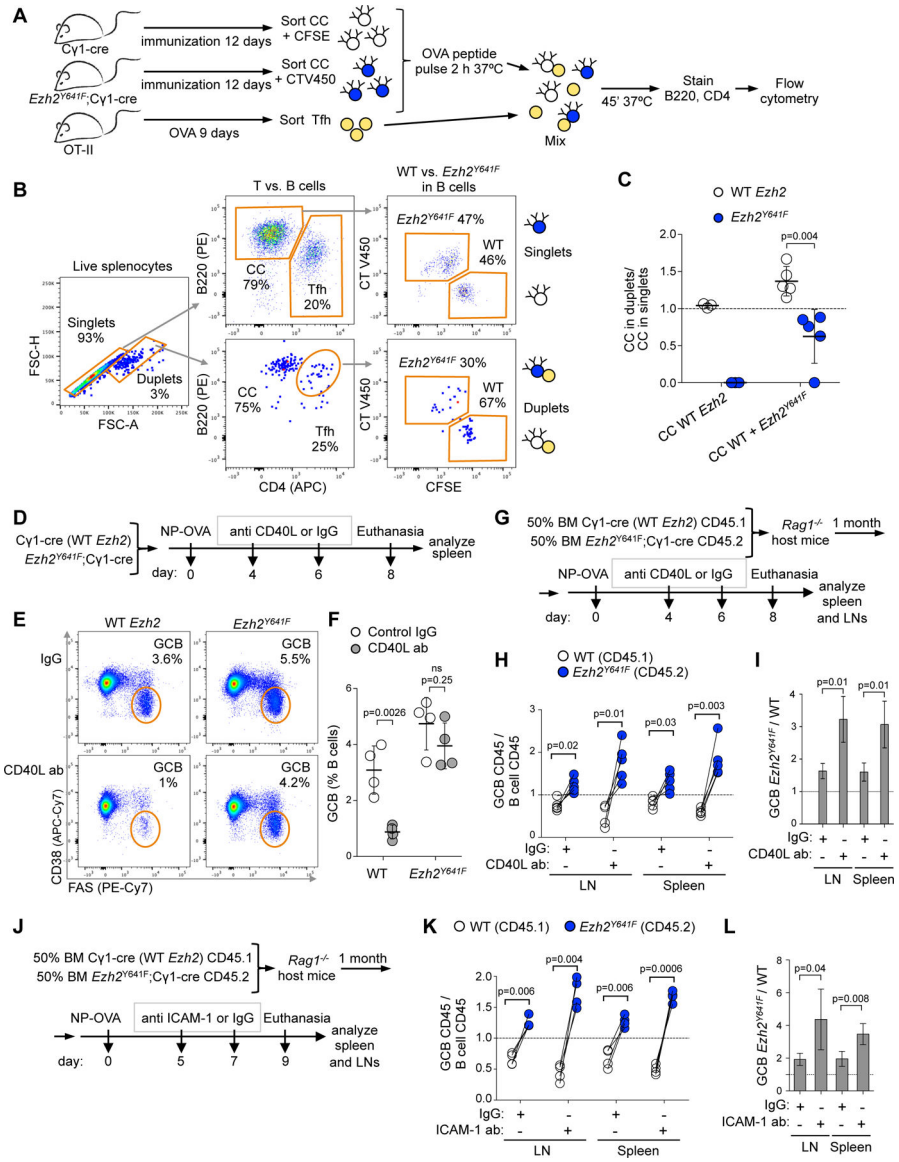


**Figure 6. Decreased interaction and dependency on Tfh cells by *Ezh2*$^{Y641F}$ GC B cells**

**A**. Five Cγ1-cre and 5 *Ezh2*$^{Y641F}$ mice were immunized with NP-CGG for 12 days and CCs ($B220^{+}CD38^{-}Fas^{+}CXCR4^{lo}CD86^{hi}$) were collected. WT CCs were stained with CFSE and *Ezh2*$^{Y641F}$ with CellTrace V450. Tfh ($CD4^{+}B220^{-}PD1^{hi}CXCR5^{hi}$) were sorted from OVA-immunized OT-II mice. CCs were pulsed *ex vivo* with OVA323–339 and then mixed with Tfh.

**B**. Tfh-CC interaction was assessed by flow cytometry-based *ex vivo* assay. Tfh-CC conjugates were identified by gating on cell duplets.

**C**. Tfh-CC duplets were normalized to CC singlets for quantification. WT CCs only, and WT CCs mixed with *Ezh2*$^{Y641F}$ CCs were incubated with Tfh. Each dot represents CCs from one mouse (n=5), mean ± SEM; unpaired t test. Results representative of 2 experiments.

Author Manuscript Author Manuscript Author Manuscript Author Manuscript

**D**. WT and *Ezh2*$^{Y641F}$ immunized mice (n=4) were treated with two doses of 100 μg anti CD40L or control IgG antibody.

**E**. Representative flow cytometry plots of %GC B cells gated on live B cells of mice groups shown in **D**.

**F**. Average percentage of GC B cells gated as shown in **E**. Each dot represents GC B cells from one mouse (n=4), mean ± SEM; unpaired t test.

**G**. Mixed chimera mice (n=4) immunized with NP-OVA were treated with anti CD40L antibody as in **D**.

**H**. Splenocytes and LN cells collected as shown in **G** were analyzed by flow cytometry, normalizing the percentage of CD45.1$^+$ GC B cells (CD38$^-$FAS$^+$) to their parental CD45.1$^+$ B cells (B220$^+$DAPI$^-$), and equivalent normalization with CD45.2$^+$ populations. Each pair of connected dots represents a mouse; paired t tests.

**I**. Ratio of *Ezh2*$^{Y641F}$ to WT GC B cells from **H**; mean ± SEM; unpaired t test.

**J**. Mixed chimera mice (n=4) immunized with NP-OVA were treated with two doses of 150 μg anti ICAM-1 or control IgG antibody.

**K**. Splenocytes and LN cells collected as shown in **J** were analyzed by flow cytometry as in **H**.

**L**. Ratio of *Ezh2*$^{Y641F}$ to WT GC B cells from **K**; mean ± SEM; unpaired t test.

Results in (**D**-**L**) representative of 2 to 4 experiments.

See also Figure S6.

Author Manuscript Author Manuscript Author Manuscript Author Manuscript

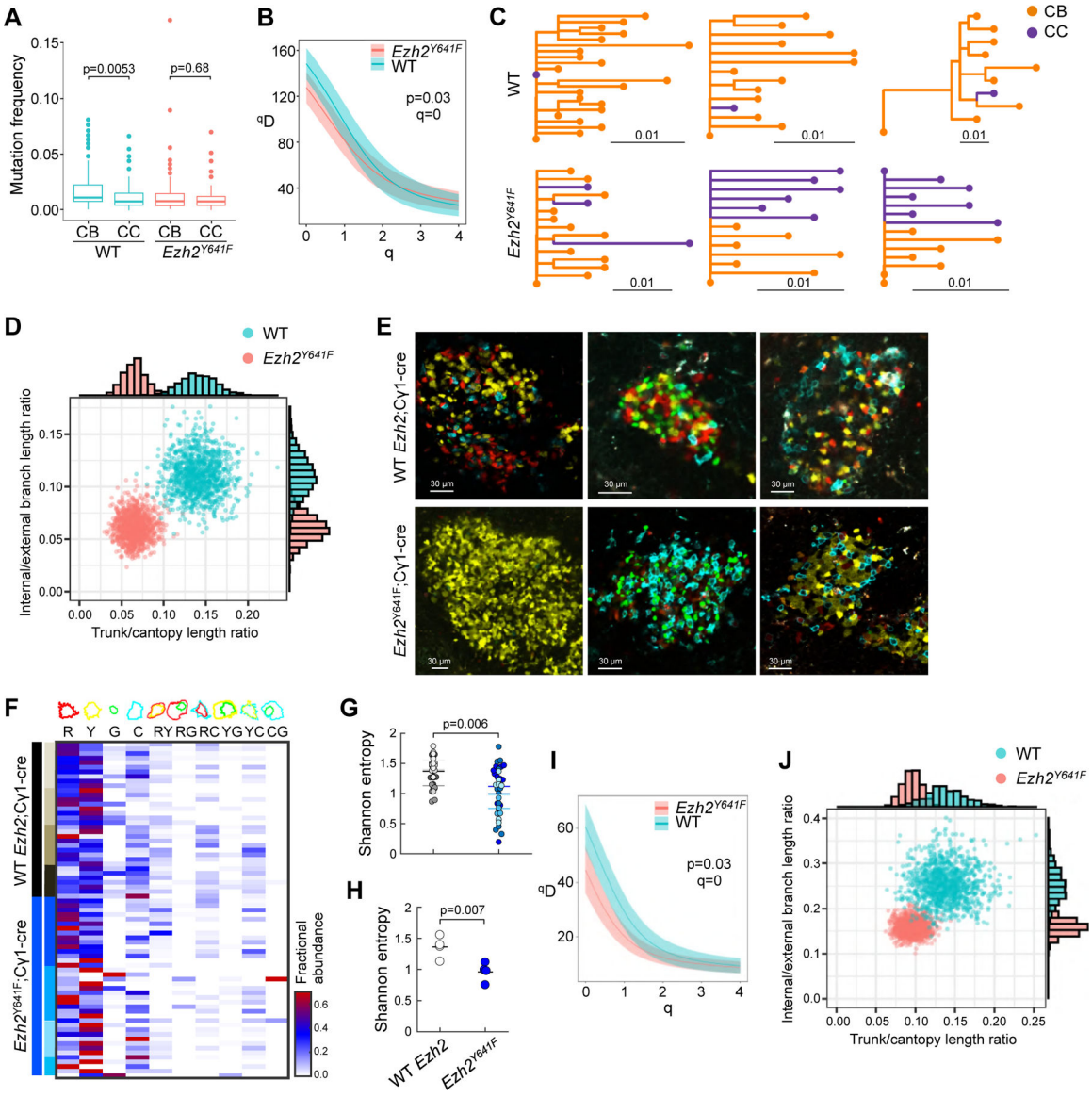


**Figure 7. *Ezh2* mutation induces reduction in clonality**

**A**. Mutation frequency of V segments (n=3 mice), measured in proportion of mismatched nucleotide sites between each V segment of each sequence and its predicted germline V segment; p values Wilcoxon rank sum test.

**B**. Diversity curves of YFP;Cγ1-cre (WT) and YFP;*Ezh2*$^{Y641F}$ mice generated through 1000 uniformly sampled bootstrap replicates.

**C**. Lineage trees of three largest WT and *Ezh2*$^{Y641F}$ YFP mice.

**D**. Distribution of 1000 bootstrap replicates showing total trunk/canopy (non-trunk) branch length ratio and internal/external branch length ratio of lineage trees obtained from WT and *Ezh2*$^{Y641F}$ YFP mice. Marginal histograms of each statistic are shown on the top and right sides.

**E**. IF confocal microscopy images of R26R-Confetti splenic GCs at day 10 post-SRBC immunization.

Author Manuscript Author Manuscript Author Manuscript Author Manuscript

**F**. Heatmap representing quantification of clonal abundance from GCs derived from 4 R26R-Confetti;Cγ1-cre and 4 R26R-Confetti;*Ezh2*$^{Y641F}$ mice. Scale from white to red denotes the fractional abundance of each clone.

**G-H**. Shannon entropy was calculated per GC (represented by dots, with each color representing GC from a different mouse, n WT=34, *Ezh2*$^{Y641F}$=39) (**G**) and for all GCs per mouse (**H**).

**I**. Diversity curves of R26R-Confetti mice generated as in **B**.

**J**. Distribution of lineage trees obtained from R26R-Confetti mice analyzed as in **D**.

See also Figure S7.

Author Manuscript Author Manuscript Author Manuscript Author Manuscript

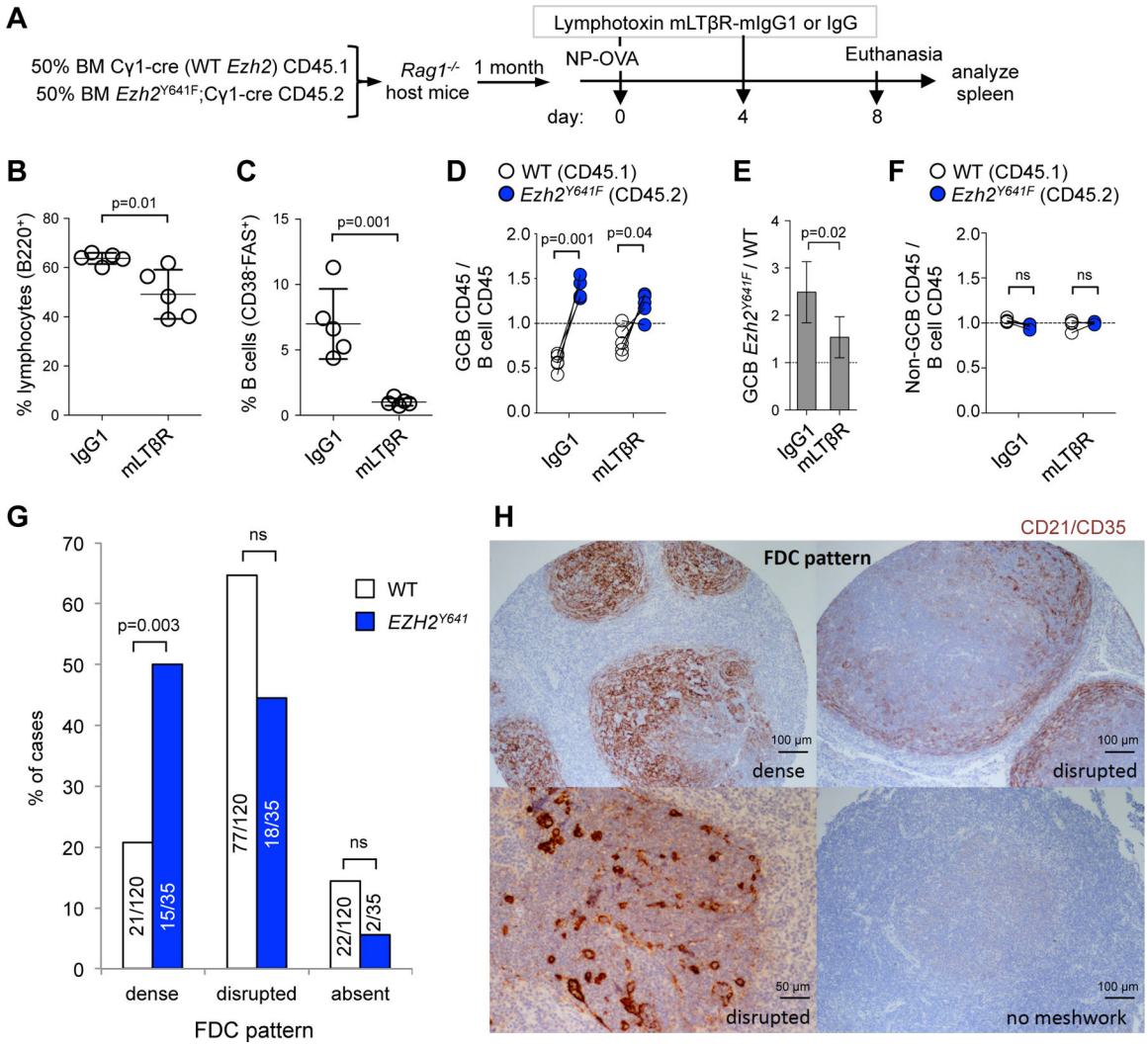


**Figure 8. *Ezh2*$^{Y641F}$ GC B cells switch from T cell to FDC dependency**

**A.** Mixed chimera mice (n=5) immunized with NP-OVA were treated with two doses of 100 µg lymphotoxin mLTβR-mIgG1 or control IgG antibody.

**B-C**. Effect of mLTβR-mIgG1 was evaluated by flow cytometry in splenic B cells (**B**) and GC B cells (**C**); data are mean (n=5) ± SEM; unpaired t test.

**D**. GC B cells collected as shown in **A** were analyzed by flow cytometry, by normalizing the percentage of CD45.1$^+$ GC B cells (CD38$^-$FAS$^+$) to their parental CD45.1$^+$ B cells (B220$^+$DAPI$^-$), and equivalent normalization with CD45.2$^+$ populations. Each pair of connected dots represents a mouse; paired t tests.

**E**. Ratio of *Ezh2*$^{Y641F}$ to WT GC B cells from **D**; mean ± SEM; unpaired t test.

**F**. Analysis of non-GC B cells (CD38$^+$FAS$^-$) was done as in **D**.

**G**. Analysis of FDC patterns in a tissue microarray with 155 grade 1 or 2 FL samples (120 WT + 35 *EZH2*$^{Y641}$); p values Fisher's exact test.

**H**. FDC patterns were clasified based on the expression of CD21/CD35 by IHC.

Author Manuscript Author Manuscript Author Manuscript Author Manuscript

## KEY RESOURCES TABLE

| REAGENT or RESOURCE | SOURCE | IDENTIFIER |
|---|---|---|
| Antibodies | | |
| Armenian hamster anti-mouse CD40L (clone MR-1) | BioXCell | Cat# BE0017 |
| Rat anti-mouse ICAM-1 (clone YN1/1.7.4) | BioXCell | Cat# BE0020 |
| Polyclonal armenian hamster IgG | BioXCell | Cat# BE0091 |
| Rat IgG2b isotype control | BioXCell | Cat# BE0090 |
| Rat anti-mouse CD16/CD32 (Fc block) | BD Biosciences | Cat# 553142 |
| Rat eFluor506 anti-B220 | ThermoFisher Scientific | Cat# 69–0452 |
| Rat APC anti-CD38 | ThermoFisher Scientific | Cat# 17–0381 |
| Rat PE anti-CXCR4 | ThermoFisher Scientific | Cat# 12–9991 |
| Rat APC anti-CD4 | ThermoFisher Scientific | Cat# 17–0041 |
| Mouse PerCP-Cy5.5 anti-CD45.1 | ThermoFisher Scientific | Cat# 45–0453 |
| Mouse PE-Cy7 anti-CD45.2 | ThermoFisher Scientific | Cat# 25–0454 |
| Armenian hamster FITC anti-PD-1 | ThermoFisher Scientific | Cat# 11–9985 |
| Rat APC anti-B220 | BD Biosciences | Cat# 553092 |
| Rat BV786 anti-B220 | BD Biosciences | Cat# 563894 |
| Hamster PE anti-FAS | BD Biosciences | Cat# 554258 |
| Hamster PE-Cy7 anti-FAS | BD Biosciences | Cat# 557653 |
| Hamster BV421 anti-FAS | BD Biosciences | Cat# 562633 |
| Rat FITC anti-CD38 | BD Biosciences | Cat# 558813 |
| Rat BV395 anti-CD38 | BD Biosciences | Cat# 740245 |
| Rat PE-Cy7 anti-CD86 | BD Biosciences | Cat# 560582 |
| Rat BV421 anti-CD86 | BD Biosciences | Cat# 564198 |
| Rat biotin anti-CXCR4 | BD Biosciences | Cat# 551968 |
| Rat biotin anti-CXCR5 | BD Biosciences | Cat# 551960 |
| Rat PE anti-IgD | BD Biosciences | Cat# 558597 |
| Rat BV510 anti-IgD | BD Biosciences | Cat# 563110 |
| Rat APC anti-IgG1 | BD Biosciences | Cat# 560089 |
| Rat BV421 anti-IgG1 | BD Biosciences | Cat# 562580 |
| Rat BUV737 anti-CD138 | BD Biosciences | Cat# 564430 |
| Rabbit AF647 anti-active caspase-3 | BD Biosciences | Cat# 560626 |
| Mouse BV421 anti-Ki67 | BD Biosciences | Cat# 562899 |
| Rat BUV395 anti-BAFF-R | BD Biosciences | Cat# 742871 |
| Rat BV650 anti-ICAM-2 | BD Biosciences | Cat# 740470 |
| Mouse BV711 anti-Ly108 | BD Biosciences | Cat# 740823 |
| Mouse AF488 anti-EZH2 | BD Biosciences | Cat# 562479 |
| Rat BV421 anti-CD35 | BD Biosciences | Cat# 740029 |
| Rat APC-Cy7 anti-B220 | BioLegend | Cat# 103224 |

Author Manuscript Author Manuscript Author Manuscript Author Manuscript

| REAGENT or RESOURCE | SOURCE | IDENTIFIER |
|---|---|---|
| Rat PE anti-B220 | BioLegend | Cat# 103208 |
| Rat APC-Cy7 anti-CD38 | BioLegend | Cat# 102728 |
| Rat PerCP-Cy5.5 anti-GL7 | BioLegend | Cat# 144610 |
| Mouse PerCP-Cy5.5 anti-FAS | BioLegend | Cat# 152610 |
| Rat APC anti-CD86 | BioLegend | Cat# 105012 |
| Rat biotin anti-CD83 | BioLegend | Cat# 121504 |
| Rat PE-Cy7 anti-CD138 | BioLegend | Cat# 142514 |
| Rat BV421 anti-CD138 | BioLegend | Cat# 142508 |
| Mouse APC-Cy7 anti-CD45.2 | BioLegend | Cat# 109824 |
| Rat PerCP-Cy5.5 anti-ICAM-1 | BioLegend | Cat# 116123 |
| Mouse AF594 anti-CD45.1 | BioLegend | Cat# 110750 |
| Mouse AF647 anti-CD45.2 | BioLegend | Cat# 109817 |
| Rat AF488 anti-IgD | BioLegend | Cat# 405717 |
| Mouse anti-human CD21 (clone 2G9) | Cell Marque | Cat# 121M |
| Rabbit AF647 anti-H3K27me3 | Cell Signaling | Cat# 12158 |
| Goat HRP-conjugated anti-mouse IgG1 | SouthernBiotech | Cat# 1070–05 |
| Goat HRP-conjugated anti-mouse IgM | SouthernBiotech | Cat# 1020–05 |
| Mouse immunoglobulin panel (IgG1, IgG2a, IgG2b, IgG3, IgA, IgM) | SouthernBiotech | Cat# 5300–01 |
| Goat anti-mouse Kappa | SouthernBiotech | Cat# 1050–01 |
| Goat anti-mouse Lambda | SouthernBiotech | Cat# 1060–01 |
| Rabbit H3K27me3 (for ChIP) | Cell Signaling | Cat# 9733 |
| Biological Samples | | |
| Sheep red blood cells | Cocalico Biologicals | Cat# 20–1334A |
| Tissue microarrays of 232 primary diagnosed FL | Kridel et al., 2016 | N/A |
| Chemicals, Peptides, and Recombinant Proteins | | |
| NP-OVAL | Biosearch Technologies | Cat# N-5051 |
| NP-CGG | Biosearch Technologies | Cat# N-5055C |
| NP-KLH | Biosearch Technologies | Cat# N-5060 |
| Alum adjuvant | ThermoFisher Scientific | Cat# 77161 |
| mLTβR (recombinant mouse Lymphotoxin beta R/TNFRSF3 Fc Chimera) | R&D Systems | Cat# 1008-LR |
| PE NP | Biosearch Technologies | Cat# N-5070 |
| NIP-haptenated FITC | M. Shlomchik lab; Anderson et al., 2007 | N/A |
| Peptide OVA323–339 | MBL International | Cat# TS-M703 |
| Biotinylated Peanut Agglutinin (PNA) | Vector Laboratories | Cat# B-1075 |
| APC streptavidin | BioLegend | Cat# 405207 |
| PE-Cy7 streptavidin | ThermoFisher Scientific | Cat# 25–4317 |
| AF488 streptavidin | BioLegend | Cat# 405235 |
| AF555 streptavidin | Invitrogen | Cat# S32355 |
| NP-BSA, ratio >20 | Biosearch Technologies | Cat# N-5050H |

Author Manuscript Author Manuscript Author Manuscript Author Manuscript

| REAGENT or RESOURCE | SOURCE | IDENTIFIER |
|---|---|---|
| NP-BSA, ratio 1–4 | Biosearch Technologies | Cat# N-5050XL |
| Critical Commercial Assays | | |
| Cytofix/Cytoperm Fixation/Permeabilization Kit | BD Biosciences | Cat# 554714 |
| Phosflow Perm Buffer III | BD Biosciences | Cat# 558050 |
| Annexin V binding buffer | BD Biosciences | Cat# 556454 |
| APC conjugated Annexin V | BD Biosciences | Cat# 550475 |
| CaspGLOW Fluorescein Active Caspase Staining Kit (FITC-VAD-FMK pan-caspase inhibitor) | BioVision | Cat# K180 |
| CD45R (B220) magnetic microbeads | Miltenyi Biotec | Cat# 130–049-501 |
| CellTrace CFSE Cell Proliferation Kit | Life Technologies | Cat# C34554 |
| CellTrace Violet Cell Proliferation Kit | Life Technologies | Cat# C34557 |
| Chromium Next GEM Single Cell 3′ GEM, Library & Gel Bead Kit | 10X Genomics | Cat# 1000128 |
| TruSeq RNA Library Preparation Kit v2 | Illumina | Cat# RS-122–2001 |
| True MicroChIP & MicroPlex Library Preparation Kit | Diagenode | Cat# C01010131 |
| Deposited Data | | |
| Raw sequencing data | This manuscript | GEO: GSE138037 |
| FL RNA-seq | Ortega-Molina et al, 2015 | SRA: SRP056293 |
| FL RNA microarray | Green et al., 2015 | GEO: GSE56311 |
| Experimental Models: Organisms/Strains | | |
| Mouse: *Ezh2*$^{Y641F}$: *Ezh2(Y641F)*$^{fl}$ knock-in | Béguelin et al., 2016 | N/A |
| Mouse: *Cγ1-cre*: B6.129P2(Cg)-Ighg1$^{tm1(cre)Cgn}$/J | The Jackson Laboratory | Stock# 010611 |
| Mouse: C57BL/6J | The Jackson Laboratory | Stock# 000664 |
| Mouse: B6.SJL-*Ptprc*$^{a}$*Pepc*$^{b}$/BoyJ | The Jackson Laboratory | Stock# 002014 |
| Mouse: *Rag1* KO: B6.129S7-*Rag1*$^{tm1Mom}$/J | The Jackson Laboratory | Stock# 002216 |
| Mouse: *R26-lox-stop-lox-YFP*: B6.129X1-*Gt(ROSA)26Sor*$^{tm1(EYFP)Cos}$/J | The Jackson Laboratory | Stock# 006148 |
| Mouse: OT-II: B6.Cg-Tg(TcraTcrb)425Cbn/J | The Jackson Laboratory | Stock# 004194 |
| Mouse: *R26R-Confetti*: *Gt(ROSA)26Sor*$^{tm1(CAG-Brainbow2.1)Cle}$/J | The Jackson Laboratory | Stock# 013731 |
| Mouse: *GFP-Myc*: B6;129-*Myc*$^{tm1Slek}$/J | The Jackson Laboratory | Stock# 021935 |
| Mouse: *R26-Fucci2aR* | Mort et al., 2014 | N/A |
| Oligonucleotides | | |
| Primers used for qChIP, see Table S3 | This manuscript | N/A |
| Primers used for RT-qPCR, see Table S3 | This manuscript | N/A |
| Primers for IgG1 and IgM PCR and sequencing (Figure 8A) | Tiller et al., 2009 | N/A |
| Software and Algorithms | | |
| FlowJo | Becton Dickinson | Version 10.5.3 |
| Fiji (ImageJ) | Schindelin et al., 2012 | http://fiji.sc/ |
| Chromium Single Cell Gene Expression | 10X Genomics | https://support.10xgenomics.com/single-cell-gene-expression/software |

Author Manuscript Author Manuscript Author Manuscript Author Manuscript

| REAGENT or RESOURCE | SOURCE | IDENTIFIER |
|---|---|---|
| Seurat | Stuart et al., 2019 | https://satijalab.org/seurat/ |
| UMAP | McInnes et al., 2018 | https://umap-learn.readthedocs.io/en/latest/ |
| Slingshot and dyno package | Saelens et al., 2019; Street et al., 2018 | https://dynverse.org/dyno/reference/index.html |
| GSEA2 v2.0.13 | Broad Institute | http://software.broadinstitute.org/gsea/index.jsp |
| CASAVA | Illumina | Version 1.8.2 |
| Trim Galore! v0.4.1 | Babraham Institute | www.bioinformatics.babraham.ac.uk/projects/trim_galore/ |
| STAR transcriptome aligner v2.5.1b | Dobin et al., 2013 | http://code.google.com/p/rna-star/ |
| featureCounts | Liao et al., 2014 | http://subread.sourceforge.net |
| DESeq2 | Love et al., 2014 | https://bioconductor.org/packages/release/bioc/html/DESeq2.html |
| PAGE algorithm | Goodarzi et al., 2009 | https://github.com/goodarzilab/PAGE |
| CompChIPseq algorithm | Blanco et al., 2019 | N/A |
| DeepTools | Ramirez et al., 2014 | https://deeptools.readthedocs.io/en/develop/content/example_gallery.html |
| Denstrip R | Jackson et al., 2008 | https://cran.r-project.org/web/packages/denstrip/index.html |
| SICER algorithm | Xu et al., 2014 | http://home.gwu.edu/~wpeng/Software.htm |
| Skyline | MacLean et al., 2010 | https://skyline.ms/wiki/home/software/Skyline/page.view?name=default |
| pRESTO v0.5.10 | Vander Heiden et al., 2014 | https://presto.readthedocs.io/en/stable/ |
| USearch v7.0.1090 | Edgar, 2010 | http://www.drive5.com/usearch |

Author Manuscript Author Manuscript Author Manuscript Author Manuscript

| REAGENT or RESOURCE | SOURCE | IDENTIFIER |
|---|---|---|
| IgBLAST v1.13.0 | Ye et al., 2013 | http://www.ncbi.nlm.nih.gov/igblast/ |
| Change-O v0.4.5 | Gupta et al., 2015; Gupta et al., 2017 | https://changeo.readthedocs.io |
| Alakazam v0.3.0 | Gupta et al., 2015; Gupta et al., 2017 | https://alakazam.readthedocs.io |
| SHazaM v0.2.0 | Yaari et al., 2013 | https://shazam.readthedocs.io |
| *dnapars* v3.697; Phylogeny Inference Package, v3.6a3 | Felsenstein J., 2002 | http://evolution.genetics.washington.edu/phylip.html |
| IgPhyML v1.1.1 | Hoehn et al., 2019 | https://igphyml.readthedocs.io |
| ggtree v1.16.0 | Yu et al., 2017; Yu et al., 2018 | https://guangchuangyu.github.io/software/ggtree/ |
| Other | | |
| Sequence processing and analysis scripts of single cell immunoglobulin somatic hypermutation | This manuscript | https://bitbucket.org/kleinstein/melnick_gcb_scripts |